Non-Newtonian Nanoflud Flow and Heat Transfer in a Microchannel filled with a Porous Medium

By

Dr. Lemi Guta

Dr. Eba Hindebu

Mr. Adugna Fita

A Final Research Report Submitted to Adama Science and Technology University

Adama, Ethiopia
July 2022

ACKNOWLEDGMENTS

First of all, we would like to acknowledge Adama Science and Technology University, office of the Vice President for Research and Technology Transfer for sponsoring the entire research finance. We would also like to express our sincerely appreciation to the office of Associate Dean for Research and Technology Transfer of School of Applied Natural Science for facilitating, supporting and encouraging from the start up to the completion of this research project.

Abstract

The heat and mass transfer characteristics as well as the hydrodynamical properties of Casson nanofluid flow through microchannels in the presence of porous media with non-uniform walls temperature have large scale utilization in industries, engineering and bio-technology. Therefore, this research project considered the analysis of Casson nanofluid flow as well as heat and mass transfer characteristics with variable viscosity. The flow was generated due to the axial pressure gradient, suction/injection and buoyancy forces. The Buongiorno's nanofluids flow model (two-phase model) was used to examine the effects of the Brownian diffusion and the thermophoresis diffusion of nanoparticles while the Darcy-Forchheimer model was considered to study the interaction between the nanofluid and the porous media. The highly non-linear partial differential equations for continuity, momentum, energy and concentration were formulated, non-dimensionalized and then solved using the implicit second order accurate finite difference method known as Keller–Box method. Accordingly, the numerical results indicated that both velocity and temperature profiles have shown an increasing behavior with increasing values of β, λ, Ec, Gt, Gc, Sc, Nt, λ_e. The concentration profile has indicated an increasing trend with increasing values of Pr, Sc and Nt. Moreover, the result revealed that C_f at both sides of the microchannel walls was large for higher vales of A, Ec, F and Re. The Nusselt number at both sides of the microchannel walls has shown an increasing pattern with increasing values of Ec, λ and Re whereas both β and λ_e have indicated opposite effects on the Nusselt number at the left and right walls of the microchannel. furthermore, the Sherwood number at both sides of the microchannel walls has shown an increasing pattern with increasing values of Ec, λ, Sc and Re.

Keywords: Microchannel; Casson fluid; Nanofluid; Porous media; Suction/injection; Variable viscosity.

TABLE OF CONTENTS

LIST OF FIGURES

List of Symbols

Symbols

a	Microchannel width	k	thermal conductivity
A	Dimensionless nanofluid pressure	Nb	Brownian motion parameter
b	Porous inertial resistance coefficient	Nt	Thermophoresis parameter
C	Chemical species concentration	P	Nanofluid pressure
C_f	Coefficient of skin friction	Pr	Prandtl number
C_p	Specific heat at constant pressure	Nu	Nusselt number
D_b	Brownian diffusion coefficient	q_w	Wall heat flux
D_T	Thermal diffusion coefficient	Re	Injection/suction Reynolds number
Ec	Eckert number	S	Porous medium shape parameter
F	Forchheimer number	Sc	Schmidt number
g	Gravitational acceleration	Sh	Sherwood number
Gc	Solutal Grashof number	T	Temperature of nanofluid
Gt	Thermal Grashof number	T_0	Cold wall temperature
h_f	Convective heat transfer coefficient	T_w	Hot wall temperature
$\vec{j}$	Mass diffusion flux	(u,v)	Velocity components
j_w	Wall mass flux	V_0	Wall suction/injection velocity
K	Permeability parameter	W	Dimensionless axial velocity
(x,y)	Cartesian coordinates	X	Dimensionless axial axis

Greek Symbols

β	Casson fluid parameter
β_1	Thermal expansion coefficient
β_2	Concentration expansion coefficient
Γ	Heat capacity ratio
λ	Dimensionless variable viscosity parameter
λ_e	Dimensionless thermal relaxation parameter
λ_c	Dimensionless concentration relaxation parameter
γ_1	Viscosity variation parameter
η	Dimensionless normal axis
θ	Dimensionless temperature
$\mu(T)$	Temperature dependent dynamic viscosity
τ_w	Wall shear stress
ρ	Nanofluid density
ϕ	Dimensionless nanoparticles concentration

CHAPTER 1

INTRODUCTION

1.1 Background of the Study

Nowadays, with increasing energy prices and a demand for energy efficiency, many efforts are made for energy saving and reduction of production costs and hence convective heat enhancement and heat storage are becoming important engineering topics related to renewable energy (Bergman et al., 2011). As a result, for the last four to five decades, many techniques have been presented to improve the efficiency in industrial equipment, especially in different heat conversion devices or heat ex-changers. This technological revolution ensured the strong industrial productivity growth which in turn has brought an improved societal quality of life world wide. In general, the goal is improving heat transfer performance of the heat ex-changers which is referred to as heat transfer rate augmentation which meliorate the overall performance of the industrial system including reducing the initial and capital costs of the heat transfer devices or heat ex-changers.

For internal fluid flows in tubes or channels, the convective heat transfer rate can be enhanced by the techniques that do not require additional external power such as refinement of flow channel geometry and fluid additives (Holman, 2010). As far as channel geometry refinement is concerned, microchannels have been identified as the most essential one to transport fluids in a miniaturization systems. To this end, for the first time the concept of micro-channels was demonstrated by Tuckerman and Pease (1981) in 1981 who achieved high heat flux removal capacity of about 800W/cm^2 within heat ex-changers by utilizing a channel with hydraulic diameter of 100μm.

Micro-channels are increasingly used in a wide range of industrial and engineering applications that span from cooling of microelectronics to bio-technological applications (Saleel et al., 2019). Therefore, in recent years a number of research literature have been communicated comprising the analysis of fluid flow and heat transfer phenomena in micro-channels. To mention few, Reddy et al. (2018) investigated the combined effects of wall slip, viscous dissipation and Joule heating on MHD electro-osmotic peristaltic motion of Casson fluid through a rotating asymmetric micro-channel. Meanwhile, the explanation of the influence of slim obstacle geometry on the flow and heat transfer in micro-channels is given by Kmiotek and Kucab-Pietal (2018).

Despite of their high heat transfer capabilities, a challenging problem in microchannels is that the higher convection heat transfer coefficient comes at the cost of greater pressure

drop per unit length and hence greater requirement of pumping power in the the microchannel flow geometries (Dewan and Srivastava, 2015). Besides, common heat transfer fluids or base fluids such as water, oils and ethylene are poor in heat transfer capabilities due to their low thermal conductivity (Kumar et al., 2014). Because of the aforementioned reasons, novel technologies with the potential of improving the fluid transport properties such as thermal conductivity of the working fluid are of great interest for flows in micro-channels once again. From this perspective, among the convection heat transfer augmentation techniques by utilization of fluid additives, the most successful one is the inclusion of nanometer-sized ($1nm = 1 \times 10^{-9} nm$) solid particles into the common base fluids.

Therefore, with continued miniaturization and increasing heat dissipation in new generations of products, there is a need for more efficient heat transfer fluids in microchannels. The term nanofluid was first pioneered by Choi (1995) to indicate that nanofluids are engineered suspension or dispersion of nanometer-sized (1nm–100nm) particles in base fluids. The flow of nanofluids in micro-channels have large scale utilization particularly as coolants in industrial and technological processes (Subramanian et al., 2020). Consequently, there are many researchers for instance (Reddy et al., 2019; Niazi and Xu, 2020) who are currently reporting their research works in line with flow and heat transfer phenomena of nanofluids in micro-channels.

Casson fluid model can be regarded as the most appropriate to industrial applications for instance, exploring the mechanism of pseudo plastic yield stress liquids, in food processing, metallurgy and drilling and bio-engineering operations (Mehmood et al., 2019). Therefore, nowadays a reasonable number of communications can be quoted highlighting Casson fluid model in the existing literature. For instance, Thammanna et al. (2017) presented the transient analysis of magnetohydrodynamic stretched flow of couple stress Casson fluid with chemical reaction. Similarly, Mahanthesh et al. (2018) addressed the boundary layer flow and heat transfer in Casson fluid submerged with dust particles over three different geometries (vertical cone, wedge and plate). The governing equations were solved by shooting method coupled with the Runge-Kutta-Fehlberg-45 integration scheme. According to their results, a rise in Casson fluid parameter enhances the fluid temperature and the magnetic field improves heat transfer rate.

From the above discussion, it can be ascertained that the analysis of Casson nanofluid flow and heat transfer phenomena in micro-channels, either due to free or forced convection has been presented. However, limited studies on mixed convection flows of nanofluids in micro-channels have been carried out. Such studies are even scarce in the presence of porous media. Therefore, this study mainly focused on investigation the Casson nanofluid flow through a micro-channel filled with a saturated porous medium together with heat transfer characteristics due to mixed convection.

1.2 Statement of the Problem

The analysis of nanofluid flow and heat transfer either due to free or forced convection in micro-channels have been presented by a significant number of scholars. Fore example very recently, Shahrestani et al. (2020) presented the numerical investigation of forced convective heat transfer and performance evaluation of Al_2O_3-water nanofluid flow inside an axisymmetric micro-channel. From their results, it was noticed that the expense of increased pressure loss for the increment of the heat transfer coefficient. They also observed that an increase in inlet velocity leads to more viscous dissipation rates and the temperature of the wall grows more intensely compared with the bulk temperature of the fluid.

Ahadi et al. (2019) presented a detailed computational fluid dynamic evaluation of heat transfer enhancement due to natural convection in micro-channel solar collectors coupled with alumina nanofluid using finite element method. Consequently, they established that the optimal heat removal is achieved at 2% nanoparticle concentration and they also observed that increasing the inclination angle of the micro-channel solar collector from 0 to $\frac{\pi}{3}$ decreased the heat removal efficiency.

The experimental and numerical study of the heat transfer enhancement potential of micro-porous channels and nanofluid was given by Delisle et al. (2019). They considered the forced convection and Darcy-Brinkman nanofluid model and the numerical solution was given by the finite element method. It was found that the temperature distribution has optimal results when nanofluid with 0.6% alumina is used. They also showed that the experimental and numerical results were in good agreement with an average relative error of 3.3%, which was determined by analyzing the temperature distribution.

Sharaf et al. (2019) presented the numerical investigation of nanofluid particle migration and convective heat transfer in micro-channels. A transient, two-way coupled hybrid Eulerian-Lagrangian model was used to characterize nanofluid flow, heat transfer and particle distribution in a micro-channel. According to the results, an increase in Reynolds number Re resulted in a lower bulk fluid temperatures and a corresponding enhancement of convective heat transfer and Nusselt number from channel walls to the fluid due to the larger temperature gradient normal to the channel wall.

However, limited studies on flow and heat transfer of Casson nanofluids in micro-channels filled with porous media have been carried out. Such studies are even scarce in the mixed convection flow. Therefore, this project mainly focuses on the mathematical investigation of unsteady flow of Casson nanofluids as well as the heat transfer phenomena due to mixed convection in micro-channels filled with porous media.

For fluid flow in micro-channels there always exists high frictional resistance of the coolants leading to generation of high temperature within the fluid and thus,the viscosity of the fluid was assumed to be erratic with temperature (Makinde, 2018). Consequently, temperature dependent variable viscosity was also considered.

1.3 Objectives of the Study

1.3.1 General Objective of the Study

The general objective of this study was to present the mathematical investigation of Casson nanofluids flow and heat transfer in a micro-channels filled with a porous medium.

1.3.2 Specific Objectives of the Study

The specific objectives of this study were to

1. formulate a mathematical model for mixed convection flow of variable viscosity Casson nanofluids in a micro-channel filled with a porous medium.
2. develop a numerical simulation in MATLAB software that can solve the mathematical model of the present flow problem and that can also be implemented to solve similar flow model problems.
3. find the convergent solutions of the velocity, temperature and concentration profiles.
4. identify the pertinent governing flow parameters.
5. describe the effects of the embedded parameters on the velocity, temperature and concentration profiles as well as on the local skin friction coefficient, the local heat transfer rate (Nusselt number) and the local mass transfer rate (Sherwood number).

1.4 Significance and Beneficiaries of the Study

The significance and beneficiaries of this study are stated as follows.

- The results that are obtained in this research project can enhance the knowledge of Casson nanofluids flow and heat transfer in micro-channels filled with porous media.
- The analysis in this research project can serve as reference for researchers on mixed convection flow of variable viscosity Casson nanofluid in a micro-channel filled with a porous medium.
- The results that are obtained in this research project for Casson nanofluids flow and heat transfer in micro-channels filled with porous media can be used as a base of ideas which can be extended to different related flow problems.
- The combination of porous media and Casson nanofluids which have high thermal conductivity may result in efficient designs for equipment meant for thermal management systems in industries. For instance, the results in this research can provide insights into designs of heat exchangers.

CHAPTER 2

REVIEW OF RELATED LITERATURE

2.1 Applications of Microchannels

A micro-channel is a medium through which fluid is used to dissipate heat from a hot surface by forcing the fluid through a passage of hydraulic diameter ranges from 1μm-100μ m (Mehendale et al., 2000). The concept of the micro-channel was demonstrated for the first time by Tuckerman and Pease (1981) in 1981 who came out with a ground breaking idea of generating high heat transfer coefficients within heat exchangers in the Stanford Electronics Laboratories. They achieved high heat flux removal capacity of about 800 W/cm^2 by utilizing a channel with hydraulic diameter of 100μm. They noted that as the hydraulic diameter of the channel decreases, the convection heat transfer coefficient increases. Micro-channel has higher heat transfer surface area to fluid volume ratio and hence it provides high heat transfer coefficient for convective heat transfer. Further more, micro-channels as heat exchangers have numerous attributes, including high thermal effectiveness, small size, low weight, low fluid inventory, and design flexibility, lower materials and manufacturing costs and light weight because of extreme compactness when compared to conventional channels and thus brought about an attractive advantage that would draw the interest of many manufacturers.

As a result, micro-channels are increasingly used in a wide range of industrial and engineering applications including electronic cooling, cooling of computer chips, chemical engineering, automotive heat exchangers, laser equipment, aerospace technology, cooling of microchips, heat sinks of MEMS based devices, drug delivery applications, DNA hybridization, chemical processing, environmental control, and energy conversion technologies, biochemical and pharmaceutical applications, bio-technologies, sensing technologies so and so on (Saleel et al., 2019). Therefore, in recent years a number of researchers have reported the analysis of fluid flow and heat transfer phenomena in micro-channels. To mention some, Reddy et al. (2018) investigated the combined effects of wall slip, viscous dissipation, and Joule heating on MHD electro-osmotic peristaltic motion of Casson fluid with heat transfer through a rotating asymmetric micro-channel. It is found that Casson fluid velocity, temperature, and heat transfer rate are enhanced with a boost in electro-osmotic force. Furthermore, Kmiotek and Kucab-Pietal (2018) used the finite element method to explain the influence of slim obstacle geometry on the flow and heat transfer in micro-channels. The results indicated that microchannels with obstacles exhibit higher heat transfer than the smooth

micro-channels.

Prameela et al. (2019) examined the steady fully developed hydromagnetic natural convection flow in a vertical micro-channel under the influence of heat generation and viscous dissipation. The exact analytical solutions for energy and momentum equations were obtained using perturbation method. Accordingly, increasing the value of heat generation parameter enhances the micro-channel slip velocity and temperature. Furthermore, it is noticed that the skin friction coefficient increases at the cold wall and decreases at the hot wall whereas the heat transfer coefficient decreases at the cold wall and increases at the hot wall with an increase in the heat generation parameter. In addition, Moon et al. (2019) performed numerical investigations into three-dimensional heat transfer enhancement in multi-harmonic wavy micro-channels. The solutions by the finite element method illustrated that as wave amplitude and Reynolds number increase the effectiveness of the device also increases and that the selection of specific material highly impacts the diffusion of heat in the solid but it is negligible on the Nusselt number for the fluid.

2.2 Casson fluids and their Applications

The Newton's law of viscosity states that the shear stress and the rate of deformation (or rate of shear strain) have linear relationship. Fluids that obey Newton's law of viscosity are known as Newtonian fluids. For examples, air, water, mercury and glycerin are Newtonian fluids. On the other hand, Non-Newtonian fluids are those fluids which do not obey the Newton's law of viscosity. That is, the shear stress and the rate of deformation (or rate of shear strain) non-linearly related. However, non-Newtonian fluids play very important role in day-to-day life as well as in various natural, industrial and engineering processes. These processes include extraction of crude oil from petroleum products, food mixing, syrup drugs, flow of blood, flow of plasma and flow of mercury amalgams, emulsion, muds, chyme, apple sauce, shampoos, soaps, sugar solution and geothermal engineering etc. (Hayat et al., 2015).

Due to the complex nature of these fluids, different models have been proposed to examine flow and heat transfer phenomenon depending on their rheological characteristics. For examples, Casson, Sisko, Prandtl, Carreau, Jeffery, Powell-Eyring fluid models etc. The rheological Casson model was pioneered by Casson (1959) in his investigation on a flow equation for pigment oil-suspensions of printing ink. Accordingly, the stress tensor is given by

$$\tau_{ij} = \begin{cases} (\mu_B + \frac{P_y}{\sqrt{2\pi}})2e_{ij}, \pi > \pi_c \\ (\mu_B + \frac{P_y}{\sqrt{2\pi_c}})2e_{ij}, \pi < \pi_c \end{cases} \tag{2.1}$$

where $\pi = e_{ij}e_{ij}$ and e_{ij} are the $(i,j)^{th}$ component of the deformation rate, π is the product of the component of the deformation rate with itself, π_c is a critical value of this product based on the non-Newtonian model, μ_B is plastic dynamic viscosity of non-Newtonian fluid, and

P_y is the yield stress of the fluid.

The Casson fluid model is also suggested as the best rheological model for blood flow and food industries such as chocolate and ketchup (Mukhopadhyay et al., 2013). Furthermore, Casson fluid model can be regarded as the most appropriate to industrial applications for instance, exploring the mechanism of pseudo plastic yield stress liquids, in food processing, metallurgy and drilling and bio-engineering operations (Mehmood et al., 2019). Therefore, nowadays a reasonable number of communications can be quoted highlighting Casson fluid model in the existing literature. For instance, Thammanna et al. (2017) presented the transient analysis of magnetohydrodynamic stretched flow of couple stress Casson fluid with chemical reaction. Moreover, the magnetohydrodynamic flow of a Casson fluid over a permeable stretching sheet in the presence of mass transfer was studied by Hari Krishna et al. (2018). From their analysis it is observed that the fluid velocity decreases with increases of the Hartmann number but increases with the Casson fluid parameter. Ullah et al. (2019) also presented the analysis of Casson fluid flow over a non-isothermal cylinder subject to suction/blowing. The numerical solution was done via the Keller box method and their findings demonstrate that as the magnitude of the Casson fluid parameter increases both the friction factor and mass transfer rate decreases whereas heat transfer rate shows the opposite effect.

2.3 Nanofluids and their Applications

Regarding to the passive heat transfer enhancement technique through fluid additives, the most successful one is the inclusion of nanometer-sized solid particles into the most common fluids, such as water, oil, and ethylene-glycol. The motivation was to improve the thermal conductivity of a mixture with a solid particle which has a higher thermal conductivity. These nanoparticles are fairly close in size to the molecules of the base fluid and, thus, can enable extremely stable suspensions with only slight gravitational settling over long periods. To this end, Choi (1995) was the first scientist in pioneering the term nanofluid in 1995 at Argonne National Laboratory of USA to indicate that nanofluids are engineered suspensions or dispersions of nanometer-sized (1nm-100nm) particles in conventional fluids (base fluids) such as water, ethylene glycol or oils to enhance thermal conductivity. Thus, nanofluids became a most promising way of fluid additives for improving the heat transfer rate.

Despite of their high heat transfer capabilities, a challenging problem in micro-channels is that the higher heat transfer coefficient comes at the cost of greater pressure drop per unit length and hence greater requirement of pumping power in the the micro-channel flow geometries (the resistance is increased due to the reduced radius of the channel). That is, high frictional resistance of the coolants due to its compactness and rapid transformation of kinetic energy of the flow to internal energy, leading to high temperature being generated within the fluid (Dewan and Srivastava, 2015). Furthermore, convectional heat transfer fluids such as water, air, oils and ethylene are poor in heat transfer capabilities due to their low

thermal conductivity (Kumar et al., 2014). Therefore, with continued miniaturization and increasing heat dissipation in new generations of products, there is a need for intensification of cooling issues in many industries like electronics, transportation, energy supply, defense and medical.

Several authors have attempted to develop convective transport models for nanofluids, among which the Buongiorno's non-homogeneous two-phase model and Tiwari and Das homogeneous single-phase model are very popular. Buongiorno (2006) developed a complete model of convective heat transport in nanofluids by considering a nanoparticle-fluid relative velocity. Although compared to other solid-liquid mixtures with particles larger than micrometers and millimeters, nanofluids behave more like a fluid, they are essentially two-phase fluids and contain some common characteristics of solid-liquids.The nanoparticles are capable of flowing effortlessly without making any blockage to themselves as they are tiny enough to act likewise to liquid molecules. The nanoparticles absolute velocity can be viewed as the sum of the base fluid velocity and a relative (slip) velocity.

Buongiorno proposed seven slip mechanisms that can produce a relative velocity between the nanoparticles and the base fluid. These are inertia, Brownian diffusion, thermophoresis, diffusiophoresis, Magnus effect, fluid drainage, and gravity. Owing to the small size of particles Buongiorno identified that only Brownian diffusion and thermophoresis are the dominant slip mechanisms in nanofluids. Brownian diffusion is the random motion of particles within the base fluid that occurs from the continuous collisions of particles and molecules of base fluid. Thermophoresis is the diffusion of particles from hotter region to colder region under the effect of temperature gradient. It is not a result of thermal convection currents but is due entirely to the presence of a temperature gradient.

Based on the experimental results Buongiorno developed four equations for two-phase non-homogeneous model for mass (two continuity equations), momentum, and heat transport in nanofluids. The momentum equation for nanofluid under boundary layer approximations remained the same as that of base fluid. Only due to the presence of nanoparticles, the Brownian motion and thermophoresis effect were exhibited through the energy and the species concentration equations. The conservation equations for nanofluids are given as follows.
Continuity equation for the nanofluid

$$\nabla \cdot V = 0 \tag{2.2}$$

where V is the nanofluid velocity. Equation (2.2) is identical to the continuity equation for a pure incompressible fluid.
The continuity equation for the nanoparticles

$$\frac{\partial \phi}{\partial t} + (V \cdot \nabla)\phi = \frac{-1}{\rho_p} \nabla \cdot J_p \tag{2.3}$$

where t is time, ϕ is nanoparticle volumetric fraction and J_p is the diffusion mass flux for the nanoparticles and represents the nanoparticle flux relative to the nanofluid velocity V. J_p can be written as the sum of only two diffusion terms namely, Brownian diffusion and thermophoresis.

$$J_p = J_{p,B} + J_{p,T} = -\rho_p(D_B \nabla\phi + \rho_p \frac{D_T}{T}\nabla T) \tag{2.4}$$

where D_B and D_T are Brownian diffusion coefficient and thermal diffusion coefficient respectively. and T is the nanofluid temperature

Now substituting equation (2.3) into equation (2.4), the continuity equation for the nanoparticles becomes

$$\frac{\partial\phi}{\partial t} + (V\cdot\nabla)\phi = \nabla\cdot(D_B\nabla\phi + \frac{D_T}{T}\nabla T) \tag{2.5}$$

Equation (2.5) states that the nanoparticles can move homogeneously with the fluid (second term of the left-hand side), but they also possess a slip velocity relatively to the fluid (right-hand side), which is due to Brownian diffusion and thermophoresis.

The momentum equation for the nanofluid with negligible external body forces is given by

$$\rho(\frac{\partial V}{\partial t} + (V\cdot\nabla)V = -\nabla P - \nabla\cdot\tau \tag{2.6}$$

where P is pressure. Note that equation (2.6) is identical to the momentum equation for a pure fluid. The stress tensor,τ can be expanded as follows by assuming Newtonian behavior and incompressible flow.

$$\tau = -\mu[\nabla\cdot V + (\nabla\cdot V)^{\mathtt{t}}] \tag{2.7}$$

where the superscript $\mathtt{t}$ indicates the transpose of $\nabla\cdot V$. If the viscosity μ is constant, equation (2.7) becomes the usual Navier-Stokes equations.

Similarly, the energy equation for nanofluid is given by

$$(\rho c)_{nf}\left(\frac{\partial T}{\partial t} + (V\cdot\nabla)T\right) = \nabla\cdot k\nabla T + (\rho c)_p\left(D_B\nabla\phi\cdot\nabla T + \frac{D_T}{T}\nabla T\cdot\nabla T\right) \tag{2.8}$$

where c_{nf} and c_p are the nanofluid specific heat, and the nanoparticle specific heat respectively and k is thermal conductivity of the nanofluid. Equation (2.8) states that heat can be transported in a nanofluid by convection (second term on the left-hand side), by conduction (first term on the right-hand side), and also by virtue of nanoparticle diffusion (second and third terms on the right-hand side). It is important to emphasize that ρc is the heat capacity of the nanofluid, and thus already accounts for the sensible heat of the nanoparticles as they move homogeneously with the fluid. Therefore, the last two terms on the right-hand side truly account for the additional contribution associated with the nanoparticle motion relative to the fluid.

Nanofluids have large scale utilization, particularly as coolants in industrial and technological processes such as electronic cooling, transportation (engine cooling/vehicle thermal

management), space and nuclear system cooling, defense applications (cooling military devices and systems), cooling in chillers and refrigerators, biomedical applications (cancer therapy), air conditioning, CPU, nuclear reactors, drug delivery, MEMS etc. (Subramanian et al., 2020). Consequently, a number of literature has been communicated in line with nanofluid flow and heat transfer phenomena in micro-channels. For instance, the influences of the thermophoresis and Brownian motion on MHD electro-osmotic Jeffrey nanofluid peristaltic flow in an asymmetric rotating micro-channel was studied by Reddy et al. (2019). It was observed that the skin-friction coefficient and Sherwood number enhance with an increase in the electro-osmosis parameter and the magnetic parameter while opposite trend observed for the Nusselt number.

Niazi and Xu (2020) studied a fully developed steady immiscible flow of nanofluid in a two-layer micro-channel in the presence of electro-kinetic effects. The Buongiorno's model was employed for describing the behavior of nanofluids and HAM was employed for the numerical computation. It was found that the Brownian diffusion, the thermophoresis diffusion, and the viscosity have significant effect on altering the flow behaviors.

2.4 Porous Media and their Applications

Another attractive passive technique for improving the convection heat transfer characteristics is the usage of porous media in micro-channels and heat exchangers. According to Mahmoudi et al. (2020) a porous medium is defined as a solid matrix which is characterized by the presence of void spaces called pores within its own volume. The porous medium can thus be modeled as a solid matrix interconnected by a network of channels, or pores, where a fluid can move. Usually both the solid matrix and the fluid are assumed to be continuous. Typical examples of natural porous media are rocks, sands, soils, cemented sandstone, biological tissues like bones, lungs and kidneys, on the other hand man made materials such as bread, sponges, cements, rubber, foams and ceramics can be considered as porous media (Mahmoudi et al., 2020). Porous media increase the contact surface area between liquid and solid surface so that the fluid flow interruptions are increasing, and therefore, the effective heat transfer rate is enhancing.

The first description of transport phenomena in a porous medium was proposed by Whitaker (1986). He formulated the basic law known as Darcy's law that governs the flow of fluids through porous media on the basis of experimental results on the flow of water through beds of sand. It also forms the scientific basis of fluid permeability used in the earth sciences, particularly in hydrogeology. It is analogous to the Fourier's law in the field of heat conduction, Ohm's law in the field of electrical networks and Fick's law in diffusion theory. One application of Darcy's law is to analyze water flow through an aquifer. Darcy's law is also used to describe oil, water, and gas flows through petroleum reservoirs. Darcy studied water flow in the soil environment and found a linear relationship between the macroscopic flow velocity,

V and the fluid pressure gradient (resistance produced by solid-fluid interaction) across the medium. Darcy's law is valid to describe flow in saturated porous media at low flow rates ($Re \ll 1$), when the flow rate and the pressure gradient have a linear relationship. This law assumes that viscous forces dominate over inertial forces in porous media and hence, inertial forces can be neglected. Thus, for steady state flow of an incompressible Newtonian fluid through a porous medium, the Darcy's law is given by

$$\nabla P = -\frac{\mu}{K} V \tag{2.9}$$

where V is Darcy velocity, P is the pressure, K is material conductivity also called Darcy permeability or specific (intrinsic) permeability of the porous medium and μ is dynamic viscosity (Kasaeian et al., 2017; Menni et al., 2018).

Despite these, the Darcy model has got limitations. Among these limitations, the main is that the Darcy model takes into account the frictional force which is offered due to the presence of solid particles to the fluid rather than the boundary and internal effects. That is, the Darcy law neglects inertia and viscous effects which are not significant for a low permeability and when the flow velocity is low. Therefore, the Darcy law does not hold well for high velocity and high permeability flows and hence to overcome this shortcomings of the Darcy law (2.9), notable equations have been developed by modifying the Darcy equation which include Forchheimer-Darcy, Brinkman-Darcy, and Darcy-Brinkman-Forchheimer.The Brinkman-Darcy model includes the viscous stresses (forces) introduced by solid boundary. In the Forchheimer-Darcy model considers nonlinear drag effect (quadratic velocity term) due to the solid matrix, which should be considered when the Reynolds number or permeability is large. In addition, by adjoining the Brinkman-Darcy and the Forchheimer-Darcy models, a generalized Darcy-Brinkman-Forchheimer (DBF) flow model has been developed. The Darcy-Forchheimer (DF) model is given by

$$\nabla P = -\frac{\mu}{K} V - \frac{\rho C_F}{\sqrt{K}} V^2 \tag{2.10}$$

where ρ is fluid density and C_F is dimensionless Forchheimer inertial resistance coefficient.

Fluid flow and heat transfer in a channel filled with porous media occur in numerous application areas. Such application areas include storage of radioactive nuclear waste, transpiration cooling, separation processes in chemical industries, filtration, transport processes in aquifers, geothermal extraction, and fiber insulation, crude oil extraction, thermal energy storage, heating and cooling in buildings, underground heat pump systems and solar energy, cooling turbine blades, cooling electronic equipment and combustion systems, heating and cooling in buildings, heating and drying process, waste treatment, radioactive nuclear waste, solar energy, float glass production, ground water movement, petroleum engineering, geology and geophysics, biomedical sciences and so on (Vafai, 2005).

Therefore, it is expected that micro-channels filled with porous media (micro-porous channels) have thermal properties similar to that of regular micro-channels while the pressure drop is lower. Micro-porous channels also have potential applications in filtration, detection of particles, cooling electronic equipment, insulation of buildings, heat and fluid exchange inside human and animal organs (tissue engineering), drying of food, etc (Waghmare et al., 2008). Moreover, such structures have been used in biological and life sciences for analyzing biological materials such as proteins, DNA, cells, embryos, and chemical reagents.

Consequently, the study of fluid flow and heat transfer in micro-channels filled with porous media has been receiving prodigious interest by many researchers nowadays. To mention few, the analysis of entropy generation and heat transport of MHD Casson fluid flow with viscous and Joule heating in an inclined porous micro-channel were presented by Gireesha et al. (2019). More over, numerical simulation for the model problem was given through Runge-Kutta-Felhberg with shooting technique. It was established that the greater values of Grashof number, heat source parameter, and Casson fluid parameter increase the velocity and temperature profiles. Velocity and temperature profile decrease with increasing values of magnetic parameter,and permeability parameter in the micro-channel.

Endalew et al. (2018) investigated the dual phase lag heat transfer effect on MHD second grade fluid flow in fully developed micro-channel filled with porous material. The governing equations of fluid velocity and temperature are solved using Laplace transform Method. The result indicated that as the second grade parameter increases fluid velocity diminishes in the all fluid flow domain but it increases as the Darcy number increases. It is also noticed that for the smaller time, the fluid velocity and fluid temperature diminish as thermal relaxation time increases but for the larger time, the fluid velocity increases but fluid temperature attains steady state as thermal retardation time increases.

Further more, Venkateswarlu et al. (2019) examined the influence of thermal radiation and heat generation on steady fully developed hydromagnetic mixed convection flow in a vertical micro-porous-channel with Darcy's law in presence of suction/injection. The influence of thermal radiation and heat generation are taken into account. Incorporating the non-dimensional variables, exact analytical solutions for the energy and momentum equations in presence of velocity slip and temperature jump are obtained. The permeability parameter reduced the fluid velocity at the micro-channel walls and enhances the fluid velocity in the central region of the micro-channel in presence of suction/injection. Also, Shashikumar et al. (2018) considered the heat transfer and entropy generation in MHD flow of Casson fluid through a porous micro-channel with thermal radiation and they investigated numerically by using fourth-fifth-order Runge-Kutta integration method along with shooting technique. Based on the numerical results, it was seen that the velocity profile increases for increasing the values of slip parameter, Hartmann number and Casson parameter. Further more, as Casson fluid parameter, Eckert number and Prandtl number increase, the temperature within the micro-channel increases.

To summarize, from the above discussions, it can be ascertained that the analysis of Casson nanofluids flow and heat transfer phenomena in micro-channels, either due to free or forced convection has been presented. However, limited studies on mixed convection flows of Casson nanofluids in micro-channels have been carried out. Such studies are even scarce in the presence of porous media. Therefore, this project mainly focuses on the mathematical investigation of Casson nanofluids flow and heat transfer phenomena due to mixed convection in micro-channels filled with porous media.

CHAPTER 3

RESEARCH METHODOLOGY

We collected certain empirical data from industries so that the parameter estimation was done for some parameters and used in the numerical computation.

3.1 Mathematical Modeling

The continuum hypothesis was assumed in the formulation of the model problems. Moreover, the conservation law of mass/matter, conservation of momentum (Newton's second law of motion), conservation of energy (first law of thermodynamics) and the law of mass balance respectively were used in deriving the continuity, momentum, energy, and species concentration equations. These governing model equations were highly non-linear partial differential equations of boundary value problems (BVPs). The boundary conditions were also formulated. Then the non-dimensional form of the governing model equations of BVPs were formulated.

3.2 Method of Solutions

The Keller-Box method which is an implicit finite difference method named after the pioneering work of Cebeci and Bradshaw (1984) was implemented to solve the flow model problem by using the Matlab software. The Keller-Box method is unconditionally stable and has a second order of accuracy with arbitrary spacing and attractive extrapolation features. It remains one of the most reliable and powerful numerical methods for nonlinear flow models that are generally parabolic in nature. The Keller-Box scheme comprises four steps:

1. Reducing the n^{th} order system of ordinary differential equations to a first order system of equations.

2. Finite difference discretization of a first order system of equations.

3. Linearizing the resulting algebraic equations by using Newton's method and writing in matrix-vector form.

4. Solving the linearized system of equations by the block-tridiagonal elimination technique.

3.3 Method of Results Analysis

The entire computational algorithms evolved from this research project were implemented using $MatlabR2012a$ software. The quantitative analysis of this study was given in which the numerical solutions were displayed via graphs for each embedded parameters. Furthermore, the qualitative analysis for the physical meaning interpretation for each graph was established in detail. That is, reasons for the obtained numerical results in line with the effects of each embedded governing flow parameters on the velocity, temperature and concentration as well as on the physical quantities of engineering interests namely skin friction coefficient, local Nusselt number and local Sherwood number were justified in detail. The results were also compared with that of the existing literature.

CHAPTER 4

MATHEMATICAL MODEL FORMULATION

4.1 The Governing Equations

Consider steady mixed convective flow of Casson nanofluid in a microchannel filled with a saturated porous medium. The microchannel is assumed to have permeable walls placed at $y = 0$ and $y = a$ as shown in figure 4.1, where a denotes the distance between the two walls.

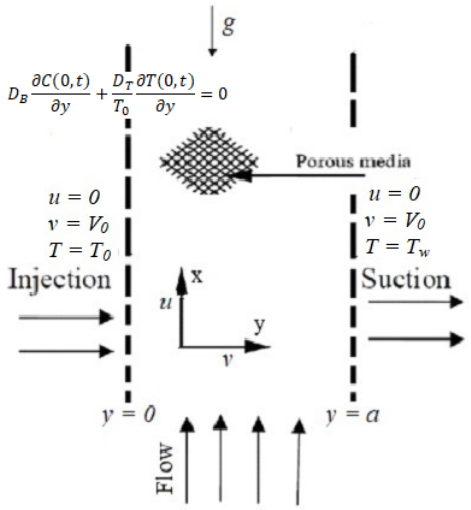

Figure 4.1: Physical Flow Model and Coordinate System

The Cattaneo-Christov diffusion model (frame-indifferent generalization of Fourier's law and Fick's law) was used in line to characterize the thermal diffusion and particle concentration diffusion with relaxation of heat flux and mass flux respectively. It was also assumed that the flow is driven by the combined actions of axial pressure gradient together with fluid body forces due to solutal and thermal buoyancy variations. Furthermore, a nanofluid injection into the microchannel take place through the left wall ($y = 0$) while a nanofluid suction out of the microchannel occurs at the right wall ($y = a$).

Also, no-slip conditions are imposed for axial velocity at the walls, and temperatures at the walls are taken to be non-uniform where the left microchannel wall is placed at temperature T_0 while the right wall is placed at temperature T_w such that $T_0 < T_w$. The nanofluid dynamic viscosity is assumed to be an exponential decreasing function of temperature and hence given as $\mu(T) = \mu_0\, e^{-\gamma_1(T-T_0)}$ where γ_1 is a viscosity variation parameter and μ_0 is the dynamic viscosity at the left wall of the microchannel.

The rheological Casson model was pioneered by Casson (1959) in his investigation on

a flow equation for pigment oil-suspensions of printing ink. Accordingly, the rheological equation of state for an isotropic and incompressible flow of a Casson fluid is given as follows.

$$\tau_{ij} = \begin{cases} (\mu_B + \frac{P_y}{\sqrt{2\pi}})2e_{ij}, \pi > \pi_c \\ (\mu_B + \frac{P_y}{\sqrt{2\pi_c}})2e_{ij}, \pi < \pi_c \end{cases} \tag{4.1}$$

where $\pi = e_{ij}e_{ij}$ and e_{ij} are the $(i,j)^{th}$ component of the deformation rate, π is the product of the component of the deformation rate with itself, π_c is a critical value of this product based on the non-Newtonian model, μ_B is plastic dynamic viscosity of non-Newtonian fluid, and P_y is the yield stress of the fluid. In the case when $\pi < \pi_c$, equation (4.1) takes the form

$$\tau_{ij} = \mu_B(1 + \frac{1}{\beta})2e_{ij} \tag{4.2}$$

where $\beta = \frac{\mu_B\sqrt{2\pi_c}}{P_y}$ is the Casson parameter. $e_{ij} = \frac{1}{2}(\frac{\partial u_i}{\partial x_j} + \frac{\partial u_j}{\partial x_i})$. For two dimensional flow, $e_{ij} = e_{xy} = \frac{1}{2}(\frac{\partial u}{\partial y} + \frac{\partial v}{\partial})) = \frac{1}{2}(\frac{\partial u}{\partial y})$. Therefore, equation (4.2) becomes,

$$\tau_{ij} = 2\mu_B(1 + \frac{1}{\beta})\frac{1}{2}(\frac{\partial u}{\partial y}) = \mu_B(1 + \frac{1}{\beta})\frac{\partial u}{\partial y} \tag{4.3}$$

Hence, the governing partial differential equations for continuity, momentum, energy and chemical species concentration are formulated under the following assumptions.

(i) The microchannel is assumed to have permeable walls with non-uniform temperatures.

(ii) The porous media is assumed to be saturated, homogeneous and isotropic.

(iii) The nanofluid flow is a two-dimensional steady laminar flow, which satisfies the no-slip boundary condition.

(iv) The interaction between the porous medium and contacting fluid was formulated using the Darcy-Forchheimer model.

(v) The nanofluid dynamic viscosity is assumed to be temperature dependent.

(vi) The nanofluid injection/suction with constant velocity V_0 at the microchannel walls is also assumed.

The axial convection terms are also assumed to be very small in the model equations and are neglected as compared to the normal convection terms and thus we have $\frac{\partial T}{\partial x} \ll \frac{\partial T}{\partial y}$, $\frac{\partial C}{\partial x} \ll \frac{\partial C}{\partial y}$, $\frac{\partial u}{\partial x} \ll \frac{\partial u}{\partial y}$.

Therefore, by considering the above assumptions and using the non-Fourier heat conduction law and non-Fick mass diffusion law, the governing equations of continuity, linear

momentum, energy and concentration under the usual Oberbeck-Boussinesq approximation are presented in the following form.

$$\frac{\partial u}{\partial x} = 0 \tag{4.4}$$

$$V_0 \frac{\partial u}{\partial y} = -\frac{1}{\rho}\frac{\partial P}{\partial x} + \frac{1}{\rho}\frac{\partial}{\partial y}\left[\mu(T)(1+\frac{1}{\beta})\frac{\partial u}{\partial y}\right] - \frac{\mu(T)(1+\frac{1}{\beta})u}{\rho K} - \frac{bu^2}{\sqrt{K}} + \beta_1 g(T-T_0) + \beta_2 g(C-C_0) \tag{4.5}$$

$$\begin{aligned} V_0 \frac{\partial T}{\partial y} = \alpha_t(\frac{\partial^2 T}{\partial y^2}) + \Gamma\left[D_B \frac{\partial C}{\partial y}\frac{\partial T}{\partial y} + \frac{D_T}{T_0}(\frac{\partial T}{\partial y})^2\right] + \frac{\mu(T)(1+\frac{1}{\beta})}{(\rho C_P)_{nf}}(\frac{\partial u}{\partial y})^2 + \lambda_E V_0^2 \frac{\partial^2 T}{\partial y^2} \\ + \frac{\mu(T)(1+\frac{1}{\beta})u^2}{(\rho C_P)_{nf} K} + \frac{\rho b u^3}{(\rho C_P)_{nf}\sqrt{K}} \end{aligned} \tag{4.6}$$

$$V_0 \frac{\partial C}{\partial y} = D_B \frac{\partial^2 C}{\partial y^2} + \frac{D_T}{T_0}\frac{\partial^2 T}{\partial y^2} + \lambda_C V_0^2 \frac{\partial^2 C}{\partial y^2} \tag{4.7}$$

With the boundary conditions:

$$\begin{aligned} &u = 0, v = V_0, T = T_0, D_B \frac{\partial C}{\partial y} + \frac{D_T}{T_0}\frac{\partial T}{\partial y} = 0, \text{ at } y = 0, \\ &u = 0, v = V_0, T = T_w, C = C_w, \text{ at } y = a \end{aligned} \tag{4.8}$$

where u is the axial velocity, V_0 is constant wall suction/injection velocity, a is the microchannel width, ρ is the nanofluid density, P is nanofluid pressure, T is the nanofluid temperature, C is the nanoparticles concentration, C_P is specific heat at constant pressure, k is thermal conductivity of the nanofluid, Γ is the heat capacity ratio which is the ratio of heat capacity of the nanoparticle and heat capacity of base fluid, K is the porous media permeability, g is gravitational acceleration, D_B is the Brownian diffusion coefficient, D_T is thermal diffusion coefficient, γ is the viscosity variation parameter, β is the Casson fluid Parameter, β_1 is the thermal expansion coefficient, β_2 is the concentration expansion coefficient, λ_E is the thermal relaxation parameter, λ_C is the concentration relaxation parameter and b is the second order dimensionless (porous inertia) resistance coefficient also known as the dimensionless Forchheimer constant such that $b = 0$ corresponds to the Darcy law.

4.2 Non-Dimensional Formulation

We define the following dimensionless variables.

$$\eta = \frac{y}{a},\ X = \frac{x}{a},\ W = \frac{\rho a u}{\mu_0},\ \theta = \frac{T-T_0}{T_1-T_0},\ \phi = \frac{C-C_0}{C_1-C_0},\ P^* = \frac{\rho a^2 P}{\mu_0^2},\ A = -\frac{\partial P^*}{\partial X},$$
$$Re = \frac{\rho V_0 a}{\mu_0},\ \lambda = \gamma(T_1-T_0),\ \lambda_e = \frac{\lambda_E V_0^2 \rho}{\mu_0},\ \lambda_c = \frac{\lambda_C V_0^2 \rho}{\mu_0},\ Da = \frac{K}{a^2},\ S = \frac{a^2}{K},$$
$$F = \frac{ba}{\rho\sqrt{K}},\ Gt = \frac{\beta_1 g \rho^2 a^3 (T_1-T_0)}{\mu_0^2},\ Gc = \frac{\beta_2 g \rho^2 a^3 (C_1-C_0)}{\mu_0^2},\ Nt = \Gamma\frac{D_T}{T_0}(T_1-T_0)\frac{\rho}{\mu_0},$$
$$Nb = \Gamma D_B (C_1-C_0)\frac{\rho}{\mu_0},\ Ec = \frac{\mu_0^2}{\rho^2 a^2 C_p (T_1-T_0)},\ Pr = \frac{\mu_0}{\rho\alpha},\ Sc = \frac{\mu_0}{\rho D_B} \tag{4.9}$$

Using the above dimensionless variables (4.9), equations (4.4)–(4.8) take the following forms.

$$\frac{\partial W}{\partial X} = 0 \tag{4.10}$$

$$Re\frac{\partial W}{\partial \eta} = A + e^{-\lambda\theta}(1+\frac{1}{\beta})\left[\frac{\partial^2 W}{\partial \eta^2} - \lambda\frac{\partial\theta}{\partial\eta}\frac{\partial W}{\partial\eta}\right] - e^{-\lambda\theta}(1+\frac{1}{\beta})S^2 W - FW^2 + Gt\theta + Gc\phi \tag{4.11}$$

$$\begin{aligned} Re\frac{\partial\theta}{\partial\eta} = (\lambda_e + \frac{1}{Pr})\frac{\partial^2\theta}{\partial\eta^2} + Nb\frac{\partial\phi}{\partial\eta}\frac{\partial\theta}{\partial\eta} + Nt(\frac{\partial\theta}{\partial\eta})^2 + Ece^{-\lambda\theta}(1+\frac{1}{\beta})(\frac{\partial W}{\partial\eta})^2 \\ + S^2 Ece^{-\lambda\theta}(1+\frac{1}{\beta})W^2 + FEcW^3 \end{aligned} \tag{4.12}$$

$$Re\frac{\partial\phi}{\partial\eta} = \frac{1}{Sc}\left[(1+\lambda_c)\frac{\partial^2\phi}{\partial\eta^2} + \frac{Nt}{Nb}\frac{\partial^2\theta}{\partial\eta^2}\right] \tag{4.13}$$

With the dimensionless boundary conditions:

$$\begin{aligned} &W = 0, \theta = 0, Nb\frac{\partial\phi}{\partial\eta} + Nt\frac{\partial\theta}{\partial\eta} = 0, \text{ at } \eta = 0, \\ &W = 0, \theta = 1, \phi = 1, \text{ at } \eta = 1 \end{aligned} \tag{4.14}$$

Re is the suction/injection Reynolds number, Gt is the Grashof number due to thermal buoyancy effect, Gc is the Grashof number due to solutal buoyancy effect, Ec is the Eckert number, Pr is the Prandtl number, A is dimensionless axial pressure gradient parameter, λ is the dimensionless viscosity variation parameter, λ_e is the dimensionless thermal relaxation parameter, λ_c is the dimensionless concentration relaxation parameter, S is the porous media shape factor parameter and F is the Forchheimer number also called the Forchheimer inertial resistance which is the second order porous media resistance parameter, Sc is the Schmidt number, Nb is the Brownian motion parameter and Nt is the thermophoresis parameter.

Indeed, from the continuity equation (4.10) $\frac{\partial W}{\partial X} = 0$, we see that W is as a function of η

only. Therefore, the governing equations (4.11)–(4.13) are ODEs with respect to η only and written as follows.

$$ReW' = A + e^{-\lambda\theta}(1+\frac{1}{\beta})(W'' - \lambda\theta' W') - e^{-\lambda\theta}(1+\frac{1}{\beta})S^2 W - FW^2 + Gt\theta + Gc\phi \quad (4.15)$$

$$Re\theta' = (\lambda_e + \frac{1}{Pr})\theta'' + Nb\phi'\theta' + Nt\theta'^2 + Ece^{-\lambda\theta}(1+\frac{1}{\beta}W'^2 + S^2 Ece^{-\lambda\theta}(1+\frac{1}{\beta})W^2 + FEcW^3 \quad (4.16)$$

$$Re\phi' = \frac{1}{Sc}\left[(1+\lambda_c)\phi'' + \frac{Nt}{Nb}\theta''\right] \quad (4.17)$$

With the dimensionless boundary conditions:

$$\begin{aligned} &W = 0, \theta = 0, Nb\phi' + Nt\theta' = 0, \text{ at } \eta = 0, \\ &W = 0, \theta = 1, \phi = 1, \text{ at } \eta = 1 \end{aligned} \quad (4.18)$$

Other physical quantities of practical significance in this study are the skin friction coefficient C_f, the local Nusselt number Nu and the local Sherwood number Sh. Therefore, the dimensionless skin friction coefficient C_f, local Nusselt number Nu and local Sherwood number Sh at the micro-channel walls are given as follows.

$$C_f = e^{-\lambda\theta}(1+\frac{1}{\beta})\left.\frac{dW}{d\eta}\right|_{\eta=0,1}, \quad Nu = -\left.\frac{d\theta}{d\eta}\right|_{\eta=0,1}, \quad Sh = -\left.\frac{d\phi}{d\eta}\right|_{\eta=0,1} \quad (4.19)$$

4.3 Numerical Procedures

4.3.1 The Keller-Box Method

The Keller-Box implicit finite difference method which was named after the pioneer work of Cebeci and Bradshaw (1984) was implemented to solve the nonlinear flow problem given in (4.15)–(4.17) with boundary conditions (4.18). This technique is unconditionally stable and has a second order accuracy with arbitrary spacing and attractive extrapolation features. The Keller-Box scheme comprises four steps:

1. Reducing the second order system of ODEs into a system of first order equations.
2. Finite difference discretization of a system of first order equations.
3. Linearizing the resulting algebraic equations by using Newton's method and writing in matrix-vector form.
4. Solving the linearized system of equations by the block-tridiagonal elimination technique.

First Order System

We write the governing second order momentum, energy and concentration equations (4.15)–(4.17) in terms of a first order equations. For this purpose let us introduce new dependent variables $f(x,\eta)$, $g(x,\eta)$, and $h(x,\eta)$ so that we have the following first order system of ODEs in terms of these new variables.

$$W' = f \tag{4.20}$$

$$\theta' = g \tag{4.21}$$

$$\phi' = h \tag{4.22}$$

$$Ref' - A - e^{-\lambda\theta}(1+\frac{1}{\beta})[f' - \lambda fg] + e^{-\lambda\theta}(1+\frac{1}{\beta})S^2W - FW^2 - Gt\theta - Gc\phi = 0 \tag{4.23}$$

$$Reg - (\lambda_e + \frac{1}{Pr})g' - Nbgh - Ntg^2 - Ece^{-\lambda\theta}(1+\frac{1}{\beta})f^2 - S^2Ece^{-\lambda\theta}(1+\frac{1}{\beta})W^2 - EcFW^3 = 0 \tag{4.24}$$

$$Reh - \frac{1}{Sc}[(1+\lambda_c)h' + \frac{Nt}{Nb}g'] = 0 \tag{4.25}$$

Therefore, the system (4.15)–(4.17) is reduced to first order system of ODEs (4.20)–(4.25).

Finite Difference Discretization

Since the governing equations have been formulated as a first order system, we can approximate all first order derivatives by the backward difference approximation and the dependent variables by two point averages. This process is called centering about $(x^i, \eta_{j-\frac{1}{2}})$.

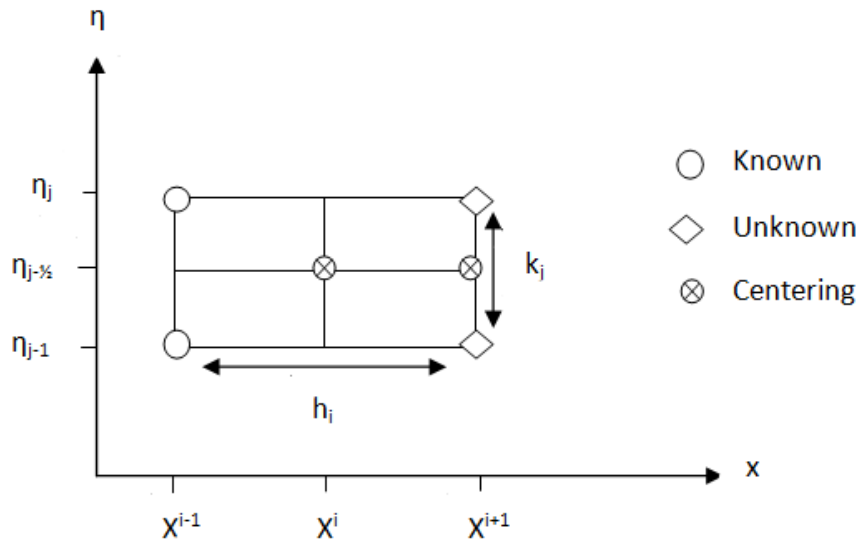

Figure 4.2: Schematic representation of finite-difference grid for the Box method

That means

$$
\begin{aligned}
&W_{j-\frac{1}{2}} = \frac{W_j + W_{j-1}}{2}, \quad \theta_{j-\frac{1}{2}} = \frac{\theta_j + \theta_{j-1}}{2}, \quad \phi_{j-\frac{1}{2}} = \frac{\phi_j + \phi_{j-1}}{2}, \\
&f_{j-\frac{1}{2}} = \frac{f_j + f_{j-1}}{2}, \quad g_{j-\frac{1}{2}} = \frac{g_j + g_{j-1}}{2}, \quad h_{j-\frac{1}{2}} = \frac{h_j + h_{j-1}}{2}, \\
&f' = \frac{f_j - f_{j-1}}{k_j}, \quad g' = \frac{g_j - g_{j-1}}{k_j}, \quad h' = \frac{h_j - h_{j-1}}{k_j}
\end{aligned} \tag{4.26}
$$

Then substituting equation (4.26) into a system of equations (4.20)–(4.25) gives the following system of equations.

$$\frac{W_j - W_{j-1}}{k_j} = \frac{1}{2}(f_j + f_{j-1}) \tag{4.27}$$

$$\frac{\theta_j - \theta_{j-1}}{k_j} = \frac{1}{2}(g_j + g_{j-1}) \tag{4.28}$$

$$\frac{\phi_j - \phi_{j-1}}{k_j} = \frac{1}{2}(h_j + h_{j-1}) \tag{4.29}$$

$$
\begin{aligned}
&Re(\frac{f_j + f_{j-1}}{2}) - A - e^{-\lambda \frac{\theta_j + \theta_{j-1}}{2}}(1 + \frac{1}{\beta})\left[\frac{f_j - f_{j-1}}{k_j} - \lambda(\frac{f_j + f_{j-1}}{2})(\frac{g_j + g_{j-1}}{2})\right] \\
&+ e^{-\lambda \frac{\theta_j + \theta_{j-1}}{2}}(1 + \frac{1}{\beta})S^2 \frac{W_j + W_{j-1}}{2} - F(\frac{W_j + W_{j-1})^2}{4} - Gt(\frac{\theta_j + \theta_{j-1}}{2}) - Gc(\frac{\phi_j + \phi_{j-1}}{2}) = 0
\end{aligned} \tag{4.30}
$$

$$
\begin{aligned}
&Re(\frac{g_j + g_{j-1}}{2}) - (\lambda_e + \frac{1}{Pr})\frac{g_j - g_{j-1}}{k_j} - Nb(\frac{g_j + g_{j-1}}{2})(\frac{h_j + h_{j-1}}{2}) - Nt(\frac{g_j + g_{j-1}}{2})^2 \\
&- Ece^{-\lambda(\frac{\theta_j + \theta_{j-1}}{2})}(1 + \frac{1}{\beta})(\frac{f_j + f_{j-1}}{2})^2 - S^2 Ece^{-\lambda(\frac{\theta_j + \theta_{j-1}}{2})}(1 + \frac{1}{\beta})(\frac{W_j + W_{j-1}}{2})^2 \\
&- EcF(\frac{W_j + W_{j-1}}{2})^3 = 0
\end{aligned} \tag{4.31}
$$

$$Re(\frac{h_j + h_{j-1}}{2}) - \frac{1}{Sc}\left[(1 + \lambda_c)(\frac{h_j - h_{j-1}}{k_j}) + \frac{Nt}{Nb}(\frac{g_j - g_{j-1}}{k_j})\right] = 0 \tag{4.32}$$

Now multiplying both sides of the above system of equations by k_j and simplifying yields,

$$W_j - f_{j-1} = \frac{k_j}{2}(f_j + f_{j-1}) \tag{4.33}$$

$$\theta_j - \theta_{j-1} = \frac{k_j}{2}(g_j + g_{j-1}) \tag{4.34}$$

$$\phi_j - \phi_{j-1} = \frac{k_j}{2}(h_j + h_{j-1}) \tag{4.35}$$

$$
\begin{aligned}
&e^{-\lambda\frac{\theta_j+\theta_{j-1}}{2}}(1+\frac{1}{\beta})(f_j-f_{j-1})-k_jRe(\frac{f_j+f_{j-1}}{2})\\
&+k_jA-k_je^{-\lambda\frac{\theta_j+\theta_{j-1}}{2}}(1+\frac{1}{\beta})\left[\lambda(\frac{f_j+f_{j-1}}{2})(\frac{g_j+g_{j-1}}{2})\right]\\
&-k_je^{-\lambda\frac{\theta_j+\theta_{j-1}}{2}}(1+\frac{1}{\beta})S^2\frac{W_j+W_{j-1}}{2}-k_jF(\frac{W_j+W_{j-1})^2}{4}\\
&+k_jGt(\frac{\theta_j+\theta_{j-1}}{2})+k_jGc(\frac{\phi_j+\phi_{j-1}}{2})=0
\end{aligned}
\tag{4.36}
$$

$$
\begin{aligned}
&(\lambda_e+\frac{1}{Pr})(g_j-g_{j-1})-k_jRe(\frac{g_j+g_{j-1}}{2})+k_jNb(\frac{g_j+g_{j-1}}{2})(\frac{h_j+h_{j-1}}{2})\\
&+k_jNt(\frac{g_j+g_{j-1}}{2})^2+k_jEce^{-\lambda(\frac{\theta_j+\theta_{j-1}}{2})}(1+\frac{1}{\beta})(\frac{f_j+f_{j-1}}{2})^2\\
&+k_jS^2Ece^{-\lambda(\frac{\theta_j+\theta_{j-1}}{2})}(1+\frac{1}{\beta})(\frac{W_j+W_{j-1}}{2})^2+k_jEcF(\frac{W_j+W_{j-1}}{2})^3=0
\end{aligned}
\tag{4.37}
$$

$$
\frac{1}{Sc}\left[(1+\lambda_c)(h_j-h_{j-1})+\frac{Nt}{Nb}(g_j-g_{j-1})\right]-k_jRe(\frac{h_j+h_{j-1}}{2})=0 \tag{4.38}
$$

Thus, a system of equations (4.33)–(4.38) represents the discretized finite difference form of the first order system of equations (4.20)–(4.25).

Newton's Method

By applying the Newton's method, we linearize the resulting algebraic equations and writing in matrix-vector form. To linearize the non-linear system of equations (4.33)–(4.38) by using the Newton's method, we introduce the following iterates.

$$
\begin{aligned}
W_j=W_j+\delta W_j,\ \ W_{j-1}=W_{j-1}+\delta W_{j-1}\\
f_j=f_j+\delta f_j,\ \ f_{j-1}=f_{j-1}+\delta f_{j-1}\\
\theta_j=\theta_j+\delta\theta_j,\ \ \theta_{j-1}=\theta_{j-1}+\delta\theta_{j-1}\\
\phi_j=\phi_j+\delta\phi_j,\ \ \phi_{j-1}=\phi_{j-1}+\delta\phi_{j-1}\\
g_j=g_j+\delta g_j,\ \ g_{j-1}=g_{j-1}+\delta g_{j-1}\\
h_j=h_j+\delta h_j,\ \ h_{j-1}=h_{j-1}+\delta h_{j-1}
\end{aligned}
\tag{4.39}
$$

Then we substitute the expressions in (4.39) into the non-linear system of equations (4.33)–(4.38) and drop the quadratic and higher-order terms in δW_j, δf_j, $\delta\theta_j$, $\delta\phi_j$, δg_j and δh_j. This procedure together with some algebraic manipulations yield the following linear tridiagonal system of equations in terms of δW_j, δf_j, $\delta\theta_j$, $\delta\phi_j$, δg_j and δh_j. The superscript i is dropped for simplicity.

$$
\delta W_j-\delta W_{j-1}-\frac{k_j}{2}(\delta f_j+\delta f_{j-1})=(r_1)_{j-\frac{1}{2}} \tag{4.40}
$$

$$
\delta\theta_j-\delta\theta_{j-1}-\frac{k_j}{2}(\delta g_j+\delta g_{j-1})=(r_2)_{j-\frac{1}{2}} \tag{4.41}
$$

$$\delta\phi_j - \delta\phi_{j-1} - \frac{k_j}{2}(\delta h_j + \delta h_{j-1}) = (r_4)_{j-\frac{1}{3}} \tag{4.42}$$

$$a_1\delta W_j + a_2\delta W_{j-1} + a_3\delta f_j + a_4\delta f_{j-1} + a_5\delta\theta_j + a_6\delta\theta_{j-1} + a_7\delta\phi_j + a_8\delta\phi_{j-1} + a_9\delta g_j + a_{10}\delta g_{j-1} = (r_4)_{j-\frac{1}{2}} \tag{4.43}$$

$$b_1\delta g_j + b_2\delta g_{j-1} + b_3\delta W_j + b_4\delta W_{j-1} + b_5\delta f_j + b_6\delta f_{j-1} + b_7\delta\theta_j + b_8\delta\theta_{j-1} + b_9\delta h_j + b_{10}\delta h_{j-1} = (r_5)_{j-\frac{1}{2}} \tag{4.44}$$

$$c_1\delta h_j + c_2\delta h_{j-1} + c_3\delta g_j + c_4\delta g_{j-1} = (r_6)_{j-\frac{1}{2}} \tag{4.45}$$

where

$(r_1)_{j-\frac{1}{2}} = W_{j-1} - W_j + k_j f_{j-\frac{1}{2}}$

$(r_2)_{j-\frac{1}{2}} = \theta_{j-1} - \theta_j + k_j g_{j-\frac{1}{2}}$

$(r_3)_{j-\frac{1}{2}} = \phi_{j-1} - \phi_j + k_j h_{j-\frac{1}{2}}$

$(r_4)_{j-\frac{1}{2}} = -k_j\lambda S^2(1+\frac{1}{\beta})(W\theta)_{j-\frac{1}{2}} + k_j FW^2_{j-\frac{1}{2}} + \lambda(1+\frac{1}{\beta})(f_j - f_{j-1})\theta_{j-\frac{1}{2}}$
$- k_j A + k_j Ref_{j-\frac{1}{2}} - k_j\lambda^2(\theta fg)_{j-\frac{1}{2}} - k_j Gt\theta_{j-\frac{1}{2}} - k_j Gc\phi_{j-\frac{1}{2}}$

$(r_5)_{j-\frac{1}{2}} = -k_j Ec\lambda S^2(1+\frac{1}{\beta})(\theta W^2)_{j-\frac{1}{2}} + k_j FEcW^3_{j-\frac{1}{2}} + k_j Ec\lambda(1+\frac{1}{\beta})(\theta f^2)_{j-\frac{1}{2}}$
$-(\lambda_e + \frac{1}{Pr})(g_j - g_{j-1}) - k_j Reg_{j-\frac{1}{2}} - k_j Nb(gh)_{j-\frac{1}{2}} - k_j Nt(g^2)_{j-\frac{1}{2}}$

$(r_6)_{j-\frac{1}{2}} = -\frac{1}{Sc}(1+\lambda_c)(h_j - h_{j-1}) + \frac{1}{Sc}\frac{Nt}{Nb}(g_j - g_{j-1}) + k_j Reh_{j-\frac{1}{2}}$

The coefficients of the momentum equation are

$$a_1 = k_j\frac{\lambda S^2}{2}(1+\frac{1}{\beta})\theta_{j-\frac{1}{2}} - k_j FW_{j-\frac{1}{2}},\ \ a_2 = a_1,$$

$$a_3 = -\frac{k_j}{2}Re + \frac{k_j}{2}\lambda^2(\theta g)_{j-\frac{1}{2}} - \lambda(1+\frac{1}{\beta})\theta_{j-\frac{1}{2}},$$

$$a_4 = \frac{k_j}{2}Re - \frac{k_j}{2}\lambda^2(\theta g)_{j-\frac{1}{2}} - \lambda(1+\frac{1}{\beta})\theta_{j-\frac{1}{2}},$$

$$a_5 = \frac{k_j}{2}\lambda^2(fg)_{j-\frac{1}{2}} + \frac{k_j}{2}\lambda S^2(1+\frac{1}{\beta})W_{j-\frac{1}{2}} - \frac{\lambda}{2}(1+\frac{1}{\beta})(f_j - f_{j-1}) + \frac{k_j}{2}Gt,\ \ a_6 = a_5,$$

$$a_7 = \frac{k_j}{2}Gc,\ \ a_8 = a_7,$$

$$a_9 = \frac{k_j}{2}\lambda^2(f\theta)_{j-\frac{1}{2}},\ \ a_{10} = a_9$$

The coefficients of the energy equation are

$$
\begin{aligned}
b_1 &= (\lambda_e + \frac{1}{Pr}) + \frac{k_j}{2}Re + \frac{k_j Nb}{2}h_{j-\frac{1}{2}} + \frac{k_j Nt}{2}g_{j-\frac{1}{2}},\\
b_2 &= -(\lambda_e + \frac{1}{Pr}) + \frac{k_j}{2}Re + \frac{k_j Nb}{2}h_{j-\frac{1}{2}} + \frac{k_j Nt}{2}g_{j-\frac{1}{2}},\\
b_3 &= k_j\lambda(1+\frac{1}{\beta})S^2 Ec(W\theta)_{j-\frac{1}{2}} - \frac{3k_j}{2}FEcW^2_{j-\frac{1}{2}},\ \ b_4 = b_3\\
b_5 &= -k_j Ec\lambda(1+\frac{1}{\beta})(f\theta)_{j-\frac{1}{2}},\ \ b_6 = b_5,,\\
b_7 &= -\frac{k_j}{2}Ec\lambda(1+\frac{1}{\beta})f^2_{j-\frac{1}{2}} + \frac{k_j}{2}Ec\lambda S^2 W^2_{j-\frac{1}{2}},\ \ b_8 = b_7,\\
b_9 &= \frac{k_j Nb}{2}g_{j-\frac{1}{2}},\ \ b_{10} = b_9
\end{aligned}
$$

The coefficients of the concentration equation are

$$
\begin{aligned}
c_1 &= \frac{1}{Sc}(1+\lambda_c) - \frac{k_j}{2}Re,\ \ c_2 = -\frac{1}{Sc}(1+\lambda_c) - \frac{k_j}{2}Re,\\
c_3 &= -\frac{1}{Sc}\frac{Nt}{Nb},\ \ c_4 = -c_3
\end{aligned}
$$

To complete the system (4.40)–(4.45), the boundary conditions (4.18) that can be satisfied exactly with no iteration (Cebeci and Bradshaw, 1984) becomes,

$$
\delta W_0 = 0,\ \ \delta\theta_0 = 0,\quad \delta\phi_0 = 0,\ \ \delta W_J = 0,\ \ \delta\theta_J = 0,\ \ \delta\phi_J = 0 \tag{4.46}
$$

The Block-tridiagonal Matrix

A block-tridiagonal matrix is a tridiagonal matrix in which the entries are not scalars but square matrices which are known as blocks. The linear system of equations (4.40)–(4.45) has a block-tridiagonal structure. That is, the complete linearized system is formulated as a block matrix system in which every element in the coefficient matrix is a matrix itself. Consequently, we represent this system by matrix-vector form as follows.

For $j = 1$, system of equations (4.40)–(4.45) becomes,

$$
\delta W_1 - \delta W_0 - \frac{1}{2}k_1(\delta f_1 + \delta f_0) = (r_1)_1
$$

$$
\delta\theta_1 - \delta\theta_0 - \frac{1}{2}k_1(\delta g_1 + \delta g_0) = (r_2)_1
$$

$$
\delta\phi_1 - \delta\phi_0 - \frac{1}{2}k_1(\delta h_1 + \delta h_0) = (r_3)_1
$$

$$
a_1\delta W_1 + a_2\delta W_0 + a_3\delta f_1 + a_4\delta f_0 + a_5\delta\theta_1 + a_6\delta\theta_0 + a_7\delta\phi_1 + a_8\delta\phi_0 + a_9\delta g_1 + a_{10}\delta g_0 = (r_4)_1
$$

$$b_1\delta g_1+b_2\delta g_0+b_3\delta f_1+b_4\delta f_0+b_5\delta W_1+b_6\delta W_0+b_7\delta\theta_1+b_8\delta\theta_0+b_9\delta h_1+b_{10}\delta h_0=(r_5)_1$$

$$c_1\delta h_1+c_2\delta h_0+c_3\delta g_1+c_4\delta g_0=(r_6)_1$$

We write as matrix-vector form as follows.

$$\begin{bmatrix} -\frac{1}{2}k_1 & 0 & 0 & 1 & 0 & 0 \\ 0 & -\frac{1}{2}k_1 & 0 & 0 & -\frac{1}{2}k_1 & 0 \\ 0 & 0 & -\frac{1}{2}k_1 & 0 & 0 & -\frac{1}{2}k_1 \\ a_4 & a_{10} & 0 & a_1 & a_9 & 0 \\ b_4 & b_2 & b_{10} & b_5 & b_1 & b_9 \\ 0 & c_4 & c_2 & 0 & c_3 & c_1 \end{bmatrix} \begin{bmatrix} \delta f_0 \\ \delta g_0 \\ \delta h_0 \\ \delta W_1 \\ \delta g_1 \\ \delta h_1 \end{bmatrix}$$

$$+ \begin{bmatrix} -\frac{1}{2}k_1 & 0 & 0 & 0 & 0 & 0 \\ 0 & 1 & 0 & 0 & 0 & 0 \\ 0 & 0 & 1 & 0 & 0 & 0 \\ a_3 & a_5 & a_7 & 0 & 0 & 0 \\ b_3 & b_7 & 0 & 0 & 0 & 0 \\ 0 & 0 & 0 & 0 & 0 & 0 \end{bmatrix} \begin{bmatrix} \delta f_1 \\ \delta\theta_1 \\ \delta\phi_1 \\ \delta W_2 \\ \delta g_2 \\ \delta h_2 \end{bmatrix} = \begin{bmatrix} (r_1)_1 \\ (r_2)_1 \\ (r_3)_1 \\ (r_4)_1 \\ (r_5)_1 \\ (r_6)_1 \end{bmatrix}$$

That is,

$$[A_1][\delta_1]+[C_1][\delta_2]=[r_1] \tag{4.47}$$

Similarly for $j=2$, system of equations (4.40)–(4.45) becomes,

$$\delta W_2-\delta W_1-\frac{1}{2}k_2(\delta f_2+\delta f_1)=(r_1)_2$$

$$\delta\theta_2-\delta\theta_1-\frac{1}{2}k_2(\delta g_2+\delta g_1)=(r_2)_2$$

$$\delta\phi_2-\delta\phi_1-\frac{1}{2}k_2(\delta h_2+\delta h_1)=(r_3)_2$$

$$a_1\delta W_2+a_2\delta W_1+a_3\delta f_2+a_4\delta f_1+a_5\delta\theta_2+a_6\delta\theta_1+a_7\delta\phi_2+a_8\delta\phi_1+a_9\delta g_2+a_{10}\delta g_1=(r_4)_2$$

$$b_1\delta g_2+b_2\delta g_1+b_3\delta f_2+b_4\delta f_1+b_5\delta W_2+b_6\delta W_1+b_7\delta\theta_2+b_8\delta\theta_1+b_9\delta h_2+b_{10}\delta h_1=(r_5)_2$$

$$c_1\delta h_2+c_2\delta h_1+c_3\delta g_2+c_4\delta g_1=(r_6)_2$$

We write as matrix-vector form as follows.

$$\begin{bmatrix} 0 & 0 & 0 & -1 & 0 & 0 \\ 0 & 0 & 0 & 0 & -\frac{1}{2}k_2 & 0 \\ 0 & 0 & 0 & 0 & 0 & -\frac{1}{2}k_2 \\ 0 & 0 & 0 & a_2 & a_{10} & 0 \\ 0 & 0 & 0 & b_6 & b_2 & b_{10} \\ 0 & 0 & 0 & 0 & c_4 & c_2 \end{bmatrix} \begin{bmatrix} \delta f_0 \\ \delta g_0 \\ \delta h_0 \\ \delta W_1 \\ \delta g_1 \\ \delta h_1 \end{bmatrix} + \begin{bmatrix} -\frac{1}{2}k_2 & 0 & 0 & 1 & 0 & 0 \\ 0 & -1 & 0 & 0 & -\frac{1}{2}k_2 & 0 \\ 0 & 0 & -1 & 0 & 0 & -\frac{1}{2}k_2 \\ a_4 & a_6 & a_8 & a_1 & a_9 & 0 \\ b_4 & b_8 & 0 & b_5 & b_1 & b_9 \\ 0 & 0 & 0 & 0 & c_3 & c_1 \end{bmatrix} \begin{bmatrix} \delta f_1 \\ \delta \theta_1 \\ \delta \phi_1 \\ \delta W_2 \\ \delta g_2 \\ \delta h_2 \end{bmatrix}$$

$$+ \begin{bmatrix} -\frac{1}{2}k_2 & 0 & 0 & 0 & 0 & 0 \\ 0 & 1 & 0 & 0 & 0 & 0 \\ 0 & 0 & 1 & 0 & 0 & 0 \\ a_3 & a_5 & a_7 & 0 & 0 & 0 \\ b_3 & b_7 & 0 & 0 & 0 & 0 \\ 0 & 0 & 0 & 0 & 0 & 0 \end{bmatrix} \begin{bmatrix} \delta f_2 \\ \delta \theta_2 \\ \delta \phi_2 \\ \delta W3 \\ \delta g_3 \\ \delta h_3 \end{bmatrix} = \begin{bmatrix} (r_1)_2 \\ (r_2)_2 \\ (r_3)_2 \\ (r_4)_2 \\ (r_5)_2 \\ (r_6)_2 \end{bmatrix}$$

That is,

$$[B_2][\delta_1] + [A_2][\delta_2] + [C_2][\delta_3] = [r_2] \tag{4.48}$$

Again for $j = J-1$, system of equations (4.40)–(4.45) becomes,

$$\delta W_{J-1} - \delta W_{J-2} - \frac{1}{2}k_{J-1}(\delta f_{J-1} + \delta f_{J-2}) = (r_1)_{J-1}$$

$$\delta \theta_{J-1} - \delta \theta_{J-2} - \frac{1}{2}k_{J-1}(\delta g_{J-1} + \delta g_{j-2}) = (r_3)_{J-1}$$

$$\delta \phi_{J-1} - \delta \phi_{J-2} - \frac{1}{2}k_{J-1}(\delta h_{J-1} + \delta h_{J-2}) = (r_4)_{J-1}$$

$$a_1\delta W_{J-1} + a_2\delta W_{J-2} + a_3\delta f_{J-1} + a_4\delta f_{J-2} + a_5\delta \theta_{J-1} + a_6\delta \theta_{J-2} + a_7\delta \phi_{J-1} + a_8\delta \phi_{J-2} + a_9\delta g_{J-1} + a_{10}\delta g_{J-2} = (r_4)_{J-1}$$

$$b_1\delta g_{J-1} + b_2\delta g_{J-2} + b_3\delta W_{J-1} + b_4\delta W_{J-2} + b_5\delta f_{J-1} + b_6\delta f_{J-2} + b_7\delta \theta_{J-1} + b_8\delta \theta_{J-2} + b_9\delta h_{J-1} + b_{10}\delta h_{J-2} = (r_5)_{J-1}$$

$$c_1\delta h_{J-1} + c_2\delta h_{J-2} + c_3\delta g_{J-1} + c_4\delta g_{J-2} = (r_6)_{J-1}$$

In matrix-vector form

$$\begin{bmatrix} 0 & 0 & 0 & -1 & 0 & 0 \\ 0 & 0 & 0 & 0 & -\frac{1}{2}k_2 & 0 \\ 0 & 0 & 0 & 0 & 0 & -\frac{1}{2}k_2 \\ 0 & 0 & 0 & a_2 & a_{10} & 0 \\ 0 & 0 & 0 & b_6 & b_2 & b_{10} \\ 0 & 0 & 0 & 0 & c_4 & c_2 \end{bmatrix} \begin{bmatrix} \delta f_{J-3} \\ \delta g_{J-3} \\ \delta h_{J-3} \\ \delta W_{J-2} \\ \delta g_{J-2} \\ \delta h_{J-2} \end{bmatrix} + \begin{bmatrix} -\frac{1}{2}k_2 & 0 & 0 & 1 & 0 & 0 \\ 0 & -1 & 0 & 0 & -\frac{1}{2}k_2 & 0 \\ 0 & 0 & -1 & 0 & 0 & -\frac{1}{2}k_2 \\ a_4 & a_6 & a_8 & a_1 & a_9 & 0 \\ b_4 & b_8 & 0 & b_5 & b_1 & b_9 \\ 0 & 0 & 0 & 0 & c_3 & c_1 \end{bmatrix} \begin{bmatrix} \delta f_{J-2} \\ \delta \theta_{J-2} \\ \delta \phi_{J-2} \\ \delta W_{J-1} \\ \delta g_{J-1} \\ \delta h_{J-1} \end{bmatrix}$$

$$+ \begin{bmatrix} -\frac{1}{2}k_2 & 0 & 0 & 0 & 0 & 0 \\ 0 & 1 & 0 & 0 & 0 & 0 \\ 0 & 0 & 1 & 0 & 0 & 0 \\ a_3 & a_5 & a_7 & 0 & 0 & 0 \\ b_3 & b_7 & 0 & 0 & 0 & 0 \\ 0 & 0 & 0 & 0 & 0 & 0 \end{bmatrix} \begin{bmatrix} \delta f_{J-1} \\ \delta \theta_{J-1} \\ \delta \phi_{J-1} \\ \delta W_J \\ \delta g_J \\ \delta h_J \end{bmatrix} = \begin{bmatrix} (r_1)_{J-1} \\ (r_2)_{J-1} \\ (r_3)_{J-1} \\ (r_4)_{J-1} \\ (r_5)_{J-1} \\ (r_6)_{J-1} \end{bmatrix}$$

That is,

$$[B_{J-1}][\delta_{J-2}] + [A_{J-1}][\delta_{J-1}] + [C_{J-1}][\delta_J] = [r_{J-1}] \tag{4.49}$$

Finally, for $j = J$, system of equations (4.40)–(4.45) also becomes,

$$\delta W_J - \delta W_{J-1} - \frac{1}{2}k_J(\delta f_J + \delta f_{J-1}) = (r_1)_J$$

$$\delta \theta_J - \delta \theta_{J-1} - \frac{1}{2}k_J(\delta g_J + \delta g_{j-1}) = (r_2)_J$$

$$\delta \phi_J - \delta \phi_{J-1} - \frac{1}{2}k_J(\delta h_J + \delta h_{J-1}) = (r_3)_J$$

$$a_1\delta W_J + a_2\delta W_{J-1} + a_3\delta f_J + a_4\delta f_{J-1} + a_5\delta \theta_J + a_6\delta \theta_{J-1} + a_7\delta \phi_J + a_8\delta \phi_{J-1} + a_9\delta g_J + a_{10}\delta g_{J-1} = (r_4)_J$$

$$b_1\delta g_J + b_2\delta g_{J-1} + b_3\delta W_J + b_4\delta W_{J-1} + b_5\delta f_J + b_6\delta f_{J-1} + b_7\delta \theta_J + b_8\delta \theta_{J-1} + b_9\delta h_J + b_{10}\delta h_{J-1} = (r_5)_J$$

$$c_1\delta h_J + c_2\delta h_{J-1} + c_3\delta g_J + c_4\delta g_J = (r_6)_J$$

In matrix-vector form

$$\begin{bmatrix} 0 & 0 & 0 & -1 & 0 & 0 \\ 0 & 0 & 0 & 0 & -\frac{1}{2}k_2 & 0 \\ 0 & 0 & 0 & 0 & 0 & -\frac{1}{2}k_2 \\ 0 & 0 & 0 & a_2 & a_{10} & 0 \\ 0 & 0 & 0 & b_4 & b_2 & b_{10} \\ 0 & 0 & 0 & 0 & c_4 & c_2 \end{bmatrix} \begin{bmatrix} \delta f_{J-2} \\ \delta g_{J-2} \\ \delta h_{J-2} \\ \delta W_{J-1} \\ \delta g_{J-1} \\ \delta h_{J-1} \end{bmatrix}$$

$$+ \begin{bmatrix} -\frac{1}{2}k_2 & 0 & 0 & 1 & 0 & 0 \\ 0 & -1 & 0 & 0 & -\frac{1}{2}k_2 & 0 \\ 0 & 0 & -1 & 0 & 0 & -\frac{1}{2}k_2 \\ a_4 & a_6 & a_8 & a_1 & a_9 & 0 \\ b_6 & b_8 & 0 & b_3 & b_1 & b_9 \\ 0 & 0 & 0 & 0 & c_3 & c_1 \end{bmatrix} \begin{bmatrix} \delta f_{J-1} \\ \delta \theta_{J-1} \\ \delta \phi_{J-1} \\ \delta W_J \\ \delta g_J \\ \delta h_J \end{bmatrix} = \begin{bmatrix} (r_1)_J \\ (r_2)_J \\ (r_3)_J \\ (r_4)_J \\ (r_5)_J \\ (r_6)_J \end{bmatrix}$$

That is,

$$[B_J][\delta_{J-1}] + [A_J][\delta_J] = [r_J] \tag{4.50}$$

Therefore, in general for $j = 1, 2, 3, ..., J-1$, we have

For $j = 1$: $[A_1][\delta_1] + [C_1][\delta_2] = [r_1]$
For $j = 2$: $[B_2][\delta_1] + [A_2][\delta_2] + [C_2][\delta_3] = [r_2]$
For $j = 3$: $[B_3][\delta_2] + [A_3][\delta_3] + [C_3][\delta_4] = [r_3]$
$\vdots$ $\vdots$
For $j = J-1$: $[B_{J-1}][\delta_{J-2}] + [A_{J-1}][\delta_{J-1}] + [C_{J-1}][\delta_J] = [r_{J-1}]$
For $j = J$: $[B_J][\delta_{J-1}] + [A_J][\delta_J] = [r_J]$

In matrix-vector form, this can be written as

$$A\delta = r \tag{4.51}$$

That is,

$$\begin{bmatrix} [A_1] & [C_1] & & & & & \\ [B_2] & [A_2] & [C_2] & & & & \\ & & & \ddots & & & \\ & & & & & & \\ & & & \ddots & & & \\ & & & & & & \\ & & & \ddots & & & \\ & & & & [B_{J-1}] & [A_{J-1}] & [C_{J-1}] \\ & & & & & [B_J] & [A_J] \end{bmatrix} \begin{bmatrix} [\delta_1] \\ [\delta_2] \\ \vdots \\ [\delta_{J-1}] \\ [\delta_J] \end{bmatrix} = \begin{bmatrix} [r_1] \\ [r_2] \\ \vdots \\ [r_{J-1}] \\ [r_J] \end{bmatrix}$$

where

$$A = \begin{bmatrix} [A_1] & [C_1] & & & & & \\ [B_2] & [A_2] & [C_2] & & & & \\ & & & \ddots & & & \\ & & & & & & \\ & & & \ddots & & & \\ & & & & & & \\ & & & \ddots & & & \\ & & & & [B_{J-1}] & [A_{J-1}] & [C_{J-1}] \\ & & & & & [B_J] & [A_J] \end{bmatrix}, \quad \delta = \begin{bmatrix} [\delta_1] \\ [\delta_2] \\ \vdots \\ [\delta_{J-1}] \\ [\delta_J] \end{bmatrix}, \quad r = \begin{bmatrix} [r_1] \\ [r_2] \\ \vdots \\ [r_{J-1}] \\ [r_J] \end{bmatrix}$$

Here, the elements of the coefficient matrix A are as follows.

$$[A_1] = \begin{bmatrix} -\frac{1}{2}k_2 & 0 & 0 & 1 & 0 & 0 \\ 0 & -1 & 0 & 0 & -\frac{1}{2}k_2 & 0 \\ 0 & 0 & -1 & 0 & 0 & -\frac{1}{2}k_2 \\ a_4 & a_6 & a_8 & a_1 & a_9 & 0 \\ b_4 & b_8 & 0 & b_5 & b_1 & b_9 \\ 0 & 0 & 0 & 0 & c_3 & c_1 \end{bmatrix}$$

$$[A_j] = \begin{bmatrix} -\frac{1}{2}k_j & 0 & 0 & 1 & 0 & 0 \\ 0 & -1 & 0 & 0 & -\frac{1}{2}k_j & 0 \\ 0 & 0 & -1 & 0 & 0 & -\frac{1}{2}k_j \\ (a_4)_j & (a_6)_j & (a_8)_j & (a_1)_j & (a_9)_j & 0 \\ (b_4)_j & (b_8)_j & 0 & (b_5)_j & (b_1)_j & (b_9)_j \\ 0 & 0 & 0 & 0 & (c_3)_j & (c_1)_j \end{bmatrix}, 2 \leq j \leq J$$

$$[B_j] = \begin{bmatrix} 0 & 0 & 0 & -1 & 0 & 0 \\ 0 & 0 & 0 & 0 & -\frac{1}{2}k_j & 0 \\ 0 & 0 & 0 & 0 & 0 & -\frac{1}{2}k_j \\ 0 & 0 & 0 & (a_2)_j & (a_{10})_j & 0 \\ 0 & 0 & 0 & (b_6)_j & (b_2)_j & (b_{10})_j \\ 0 & 0 & 0 & 0 & (c_4)_j & (c_2)_j \end{bmatrix}, 2 \leq j \leq J$$

$$[C_j] = \begin{bmatrix} -\frac{1}{2}k_j & 0 & 0 & 0 & 0 & 0 \\ 0 & 1 & 0 & 0 & 0 & 0 \\ 0 & 0 & 1 & 0 & 0 & 0 \\ (a_3)_j & (a_5)_j & (a_7)_j & 0 & 0 & 0 \\ (b_3)_j & (b_7)_j & 0 & 0 & 0 & 0 \\ 0 & 0 & 0 & 0 & 0 & 0 \end{bmatrix}, 1 \leq j \leq J-1$$

The elements of δ and that of r in equation (4.51) are also given as follows.

$$[\delta_1] = \begin{bmatrix} \delta f_0 \\ \delta g_0 \\ \delta h_0 \\ \delta W_1 \\ \delta g_1 \\ \delta h_1 \end{bmatrix}, [\delta_j] = \begin{bmatrix} \delta f_{j-1} \\ \delta \theta_{j-1} \\ \delta \phi_{j-1} \\ \delta W_j \\ \delta g_j \\ \delta h_j \end{bmatrix}, 2 \leq j \leq J \quad \text{and} \quad [r_j] = \begin{bmatrix} (r_1)_{j-\frac{1}{2}} \\ (r_2)_{j-\frac{1}{2}} \\ (r_3)_{j-\frac{1}{2}} \\ (r_4)_{j-\frac{1}{2}} \\ (r_5)_{j-\frac{1}{2}} \\ (r_6)_{j-\frac{1}{2}} \end{bmatrix}, 1 \leq j \leq J$$

The Block Tridiagonal Elimination Technique

The coefficient matrix A in equation (4.51) is known as the block-tridiagonal matrix since its elements on the main three diagonals are square matrices and all other elements are zero. To solve the system (4.51) by using the block elimination technique, we assume that A is nonsingular so that it can be factored into the form:

$$A = LU \tag{4.52}$$

where

$$L = \begin{bmatrix} [\alpha_1] & & & & \\ [B_2] & [\alpha_2] & & & \\ & \ddots & & & \\ & & \ddots & [\alpha_{J-1}] & \\ & & & [B_J] & [\alpha_J] \end{bmatrix} \quad \text{and} \quad U = \begin{bmatrix} [I] & [\Gamma_1] & & & \\ & [I] & [\Gamma_2] & & \\ & & \ddots & & \\ & & \ddots & [\Gamma_{J-1}] & \\ & & & & [I] \end{bmatrix}$$

$[I]$ is the identity matrix of order 6 and $[\alpha_j]$, and $[\Gamma_j]$ are 6×6 matrices whose elements can be determined through two sweeps as follows.

1. The Forward Sweep: $LY = r$

From equation (4.52), we have $[\alpha_1] = [A_1]$, $[\Gamma_1] = [A_1^{-1}][C_1]$.
For $j = 2,3,4,...,J$ we have also $[\alpha_j] = [A_j] - [B_j][\Gamma_{j-1}]$, and $[\Gamma_j] =]A_j^{-1}][C_j]$.
Substituting (4.52) into (4.51) yields,

$$LU\delta = r \tag{4.53}$$

Now let us define

$$U\delta = Y \tag{4.54}$$

Then (4.53) becomes,

$$LY = r \tag{4.55}$$

where, $Y = \begin{bmatrix} [y_1] \\ [y_2] \\ \vdots \\ [y_{J-1}] \\ [y_J] \end{bmatrix}$, where $[y_J]$ is 6×1 column matrices.

Then from (4.55), we see that $[Y_1] = [\alpha_1^{-1}][r_1] = [A_1^{-1}][r_1]$.
For $j = 2,3,4,...,J$, we have also $[Y_j] = [A_j^{-1}][r_j - B_j Y_{j-1}]$.

Therefore, from the forward sweep we have:

- $[\alpha_1] = [A_1]$, $[\Gamma_1] = [A_1^{-1}][C_1]$ and $[Y_1] = [A_1^{-1}][r_1]$.
- For $j = 2,3,4,...,J$, $[\alpha_j] = [A_j] - [B_j][\Gamma_{j-1}]$, $[\Gamma_j] =]A_j^{-1}][C_j]$, and $[Y_j] = [A_j^{-1}][r_j - B_j Y_{j-1}]$.

2. The Backward Sweep: $U\delta = Y$

From (4.55) we have:

- For $j = J$, we have, $[\delta_j] = [Y_j]$
- For $j = J-1, J-2, ..., 1$, we have $[\delta_j] = [Y_j] - [\Gamma_j][\delta_{j+1}]$

Once the elements of δ are found, system of equations (4.40)–(4.45) can be used to find the $(i+1)^{th}$ iteration in (4.52). These calculations are repeated until some convergence criterion is satisfied. In laminar boundary layer flow calculations, the wall shear stress parameter, $f(0)$, is usually used as the convergence criterion Cebeci and Bradshaw (1984). This might be the case, because in boundary layer flow calculations, it is found that the greatest error commonly appears in the wall shear stress parameter, $f(0)$. Hence, these calculations are stopped when $|\delta f_0^{(i)}| < \varepsilon_1$, where ε_1 is small prescribed value.

4.3.2 The Initial Guesses/The Starting Conditions

In order to start and proceed with the numerical computation, it is necessary to make initial guesses for the functions W, f, θ, g, ϕ and h across the microchannel flow between $\eta = 0$ and $\eta = 1$. It should be noted that there is a great freedom to choose initial guesses and also there are some fundamental rules which direct us to choose the values of the governing parameter in most efficient way. Therefore, initial guesses for the velocity, temperature and concentration fields are taken in such a way that they satisfy the boundary conditions given in (4.18).

The initial guesses can be obtained through trial and error and moreover, different guesses for the initial value profiles will give the same final result except that the iteration count and the computation time may be more or less Cebeci and Bradshaw (1984).

Accordingly, we assume:

$$W(\eta) = \frac{3}{2}\eta - \frac{1}{2}\eta^2 \tag{4.56}$$

Differentiating (4.56) with respect to η gives,

$$f(\eta) = \frac{3}{2} - \eta \tag{4.57}$$

Similarly, we also assume:

$$\theta(\eta) = 2\eta - \eta^2 \tag{4.58}$$

Therefore, differentiating (4.58) with respect to η yields,

$$g(\eta) = 2(1-\eta) \tag{4.59}$$

Finally, we assume:

$$\phi(\eta) = -2\eta + \eta^2 \tag{4.60}$$

Thus, differentiating (4.60) with respect to η gives,

$$h(\eta) = 2(\eta - 1) \tag{4.61}$$

Hence, these initial guesses were used as starting conditions in numerically solving the developed linear first order system of equations (4.40)—(4.45.

The step size $\Delta\eta = 0.01$ and $\Delta\zeta = 0.01$ were used to obtain the convergent numerical solutions with $\eta_{max} = 10.0$, $\zeta_{max} = 6.0$ and the accuracy of tolerance error $\varepsilon = 10^{-5}$.
The Keller-Box method used in this research project was programmed in the software known as $MatlabR2012a$.

CHAPTER 5

RESULTS AND DISCUSSIONS

5.1 The Velocity, Temperature and Concentration Profiles

Figures 5.1(a), 5.2(b) and 5.3(a) portray the effects of the Casson fluid parameter β on the nanofluid velocity, temperature and concentration profiles. Accordingly, figures 5.1(a) and 5.2(b) revealed that both the nanofluid velocity and temperature profiles within the microchannel core region increase. This is the case because as β increases, the yield stress dominates the dynamic viscosity of the nanofluid. It is noteworthy that the fluid tends to behave as a Newtonian fluid as $\beta \to \infty$. this result is similar to the findings of Reddy et al. (2018) and Roja et al. (2021). The opposite trend was observed on the concentration profile for increasing values of β as depicted in figure 5.3(a). Figures 5.2(a) and 5.2(b) display

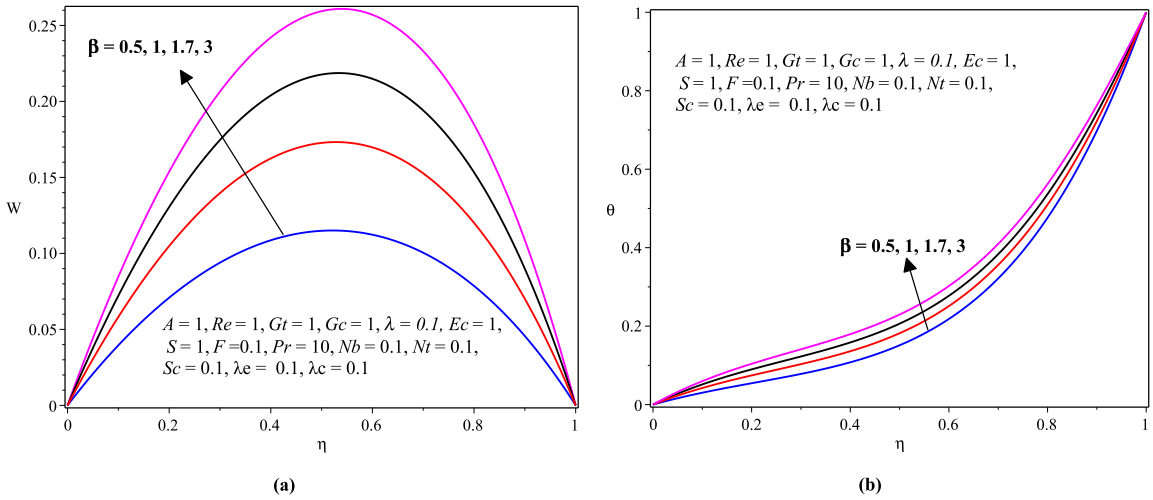

Figure 5.1: **(a)** Velocity and **(b)** Temperature profiles with varying β

that as the dimensionless variable viscosity parameter λ increases a significant rise in the nanofluid velocity and temperature profiles is observed. This is the case because an increase in λ reduces the nanofluid viscosity since $\mu(\theta) = \mu_0 e^{-\lambda\theta}$. So, the nanofluid becomes less viscous and hence friction between nanofluid layers decrease due to which velocity remains at higher levels for higher values of λ. Mahmoudi et al. (2020) reported a similar result. However, increasing the values of λ decreases the concentration profile as indicated in figure 5.3(b).

Figures 5.4(a), 5.4(b), 5.5(a) and 5.5(b) display the effects of the thermal Grashof number Gt and the solutal Grashof number Gc on velocity and temperature profiles. From the figures,

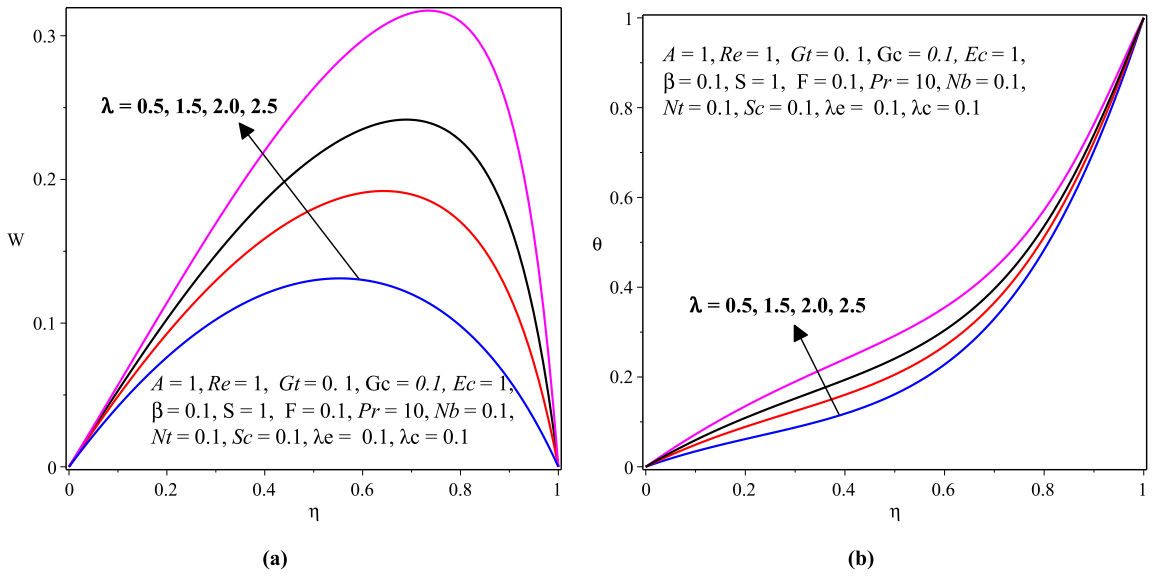

Figure 5.2: **(a)** Velocity and **(b)** Temperature profiles with varying λ

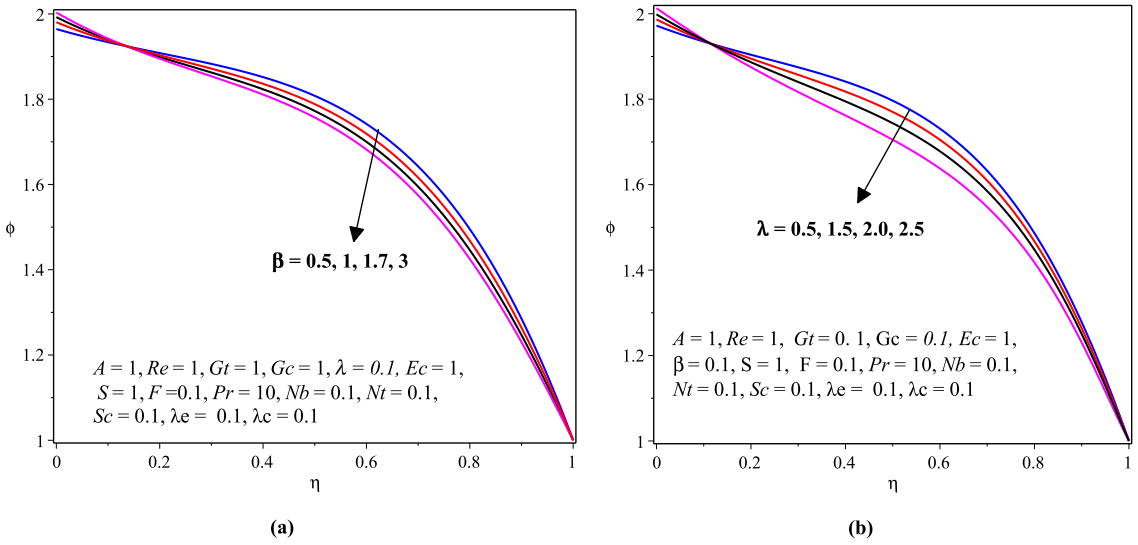

Figure 5.3: Effects of **(a)** β and **(b)** λ on Concentration profile

it can be noticed that both velocity and temperature profiles increase with *Gt* and *Gc*. This is the case because as the values of *Gt* and *Gc* enhanced, the body forces acting on the fluid (thermal and solutal buoyancy forces) also get enhanced which also enhance the velocity that in turn increase the viscous heating and hence increasing the nanofluid temperature. The opposite scenario is demonstrated in figures 5.6(a) and 5.6(b) for the concentration profile due to the fact that a small temperature increment will cause a very small decrement in concentration which is also known as the cross-diffusion effect.

Figures 5.7(a) and 5.7(b) are graphs that display the effects of the thermophoresis parameter *Nt* on the velocity and temperature profiles. Accordingly, the larger values of *Nt* leads to a significant increase in the velocity and temperature profiles. Physically, thermophoresis is a mechanism in which small particles are pulled away from hot surface to cold one and

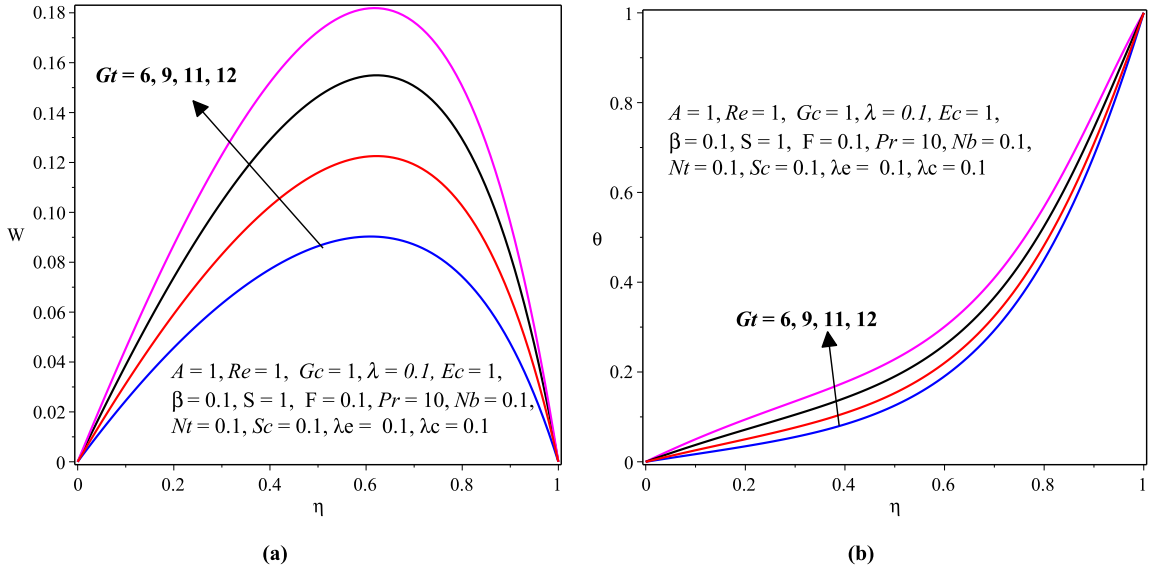

Figure 5.4: **(a)** Velocity and **(b)** Temperature profiles with varying *Gt*

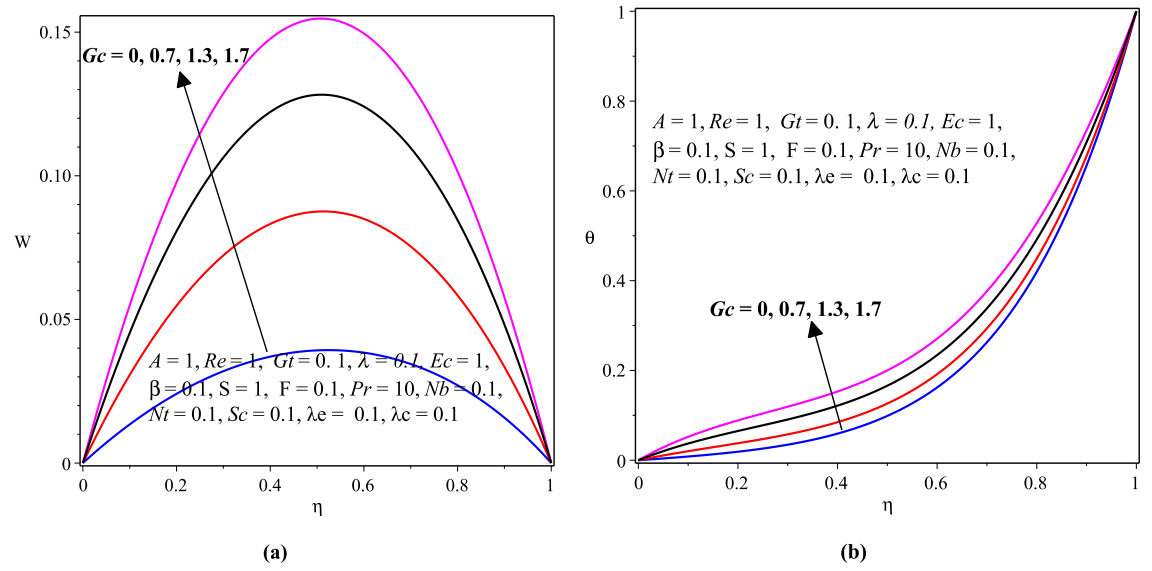

Figure 5.5: **(a)** Velocity and **(b)** Temperature profiles with varying *Gc*

thus, figures 5.7(a) and 5.7(b) declare that as the value of *Nt* enhances, both the velocity and temperature profiles also enhance. The reason behind this argument is that an enhancement in *Nt* yields a stronger thermophoretic force which allows deeper migration of nanoparticles from hot surface to cold fluid resulting in higher fluid temperature which in turn results in higher fluid velocity. The thermophoresis parameter *Nt* also has indicated the same effect on the concentration profile as shown in figure 5.9(a).

Figure 5.8(a) and 5.8(b) is a graph that display the effect of the Brownian motion parameter *Nb* on the velocity and temperature profiles. The Brownian motion is an arbitrary disorganized motion of nanoparticles dispersed in the base fluid resulting from their collision with moving molecules of the base fluid. Consequently, the velocity and temperature pro-

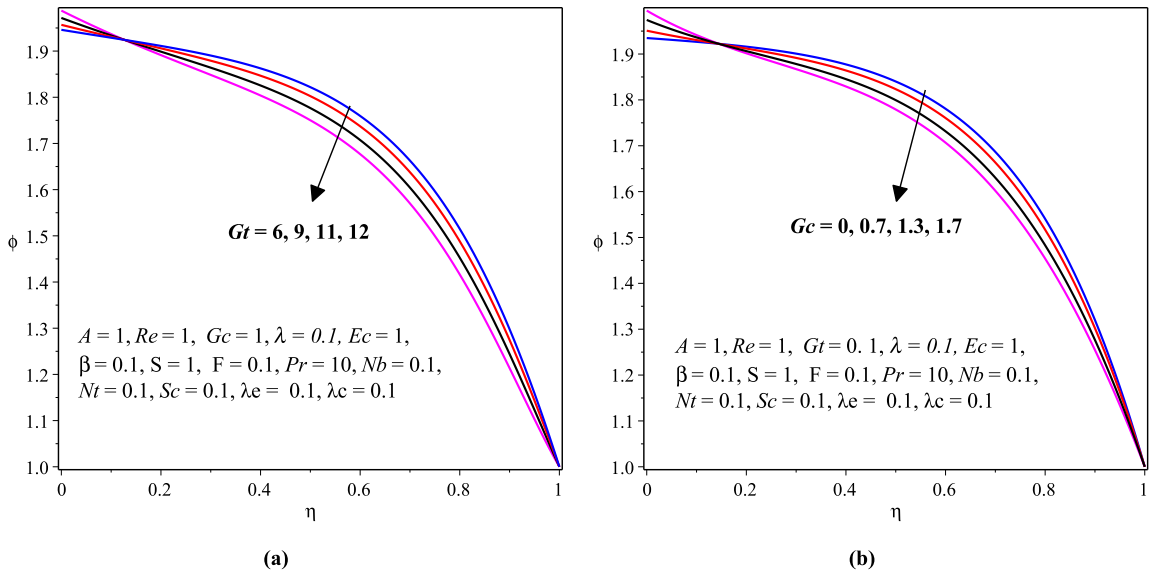

Figure 5.6: Effects of **(a)** *Gt* and **(b)** *Gc* on Concentration profile

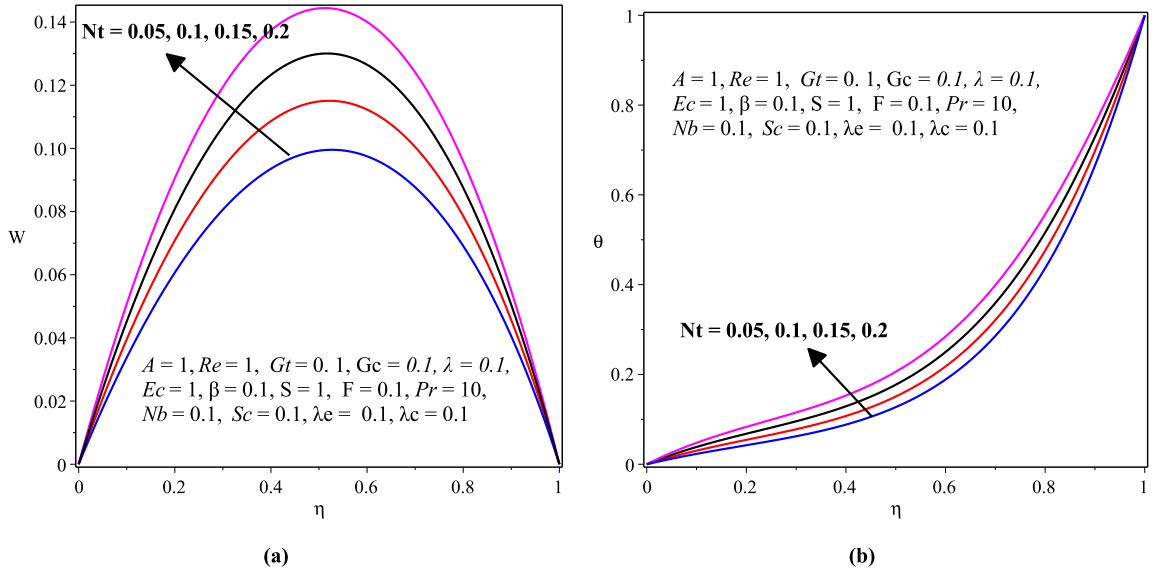

Figure 5.7: **(a)** Velocity and **(b)** Temperature profiles with varying *Nt*

files show a decreasing behavior with increasing values of the Brownian diffusion parameter *Nb* as shown in figure 5.8(a) and 5.8(b). The argument behind this result is that when the magnitudes of *Nb* increases, the random motion and also collision of the nanoparticles in the fluid increase which retards the fluid velocity that in turn decreases the fluid temperature. Similarly, the concentration profile decreases with *Nb* as shown in 5.9(b). The reason may be when the magnitudes of *Nb* increases, the random motion of the nanoparticles in the fluid increases resulting in the reduction of the concentration of the nanoparticles in the fluid.

Figures 5.10(a) and 5.10(b) displays that the Schmidt number *Sc* has a rising effect on the velocity and temperature profiles. Similarly, figure 5.11(a) indicates that the concentration profile increases with *Sc*. Physically, larger values of Schmidt number *Sc* indicate less mass

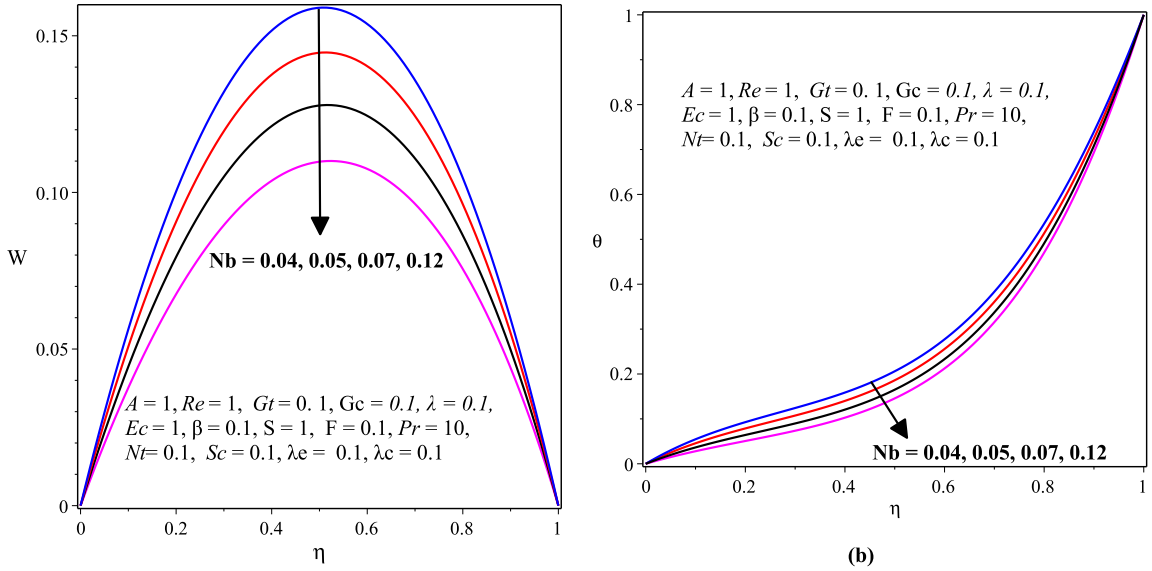

Figure 5.8: **(a)** Velocity and **(b)** Temperature profiles with varying *Nb*

diffusion which causes the concentration of nanoparticles to remain larger in the fluid. Figure 5.11(b) portrays the effect of the dimensionless concentration relaxation parameter λ_c on the concentration profile. As it can be seen from the graph, the concentration profile shows a decreasing behaviour with increasing values of λ_c.

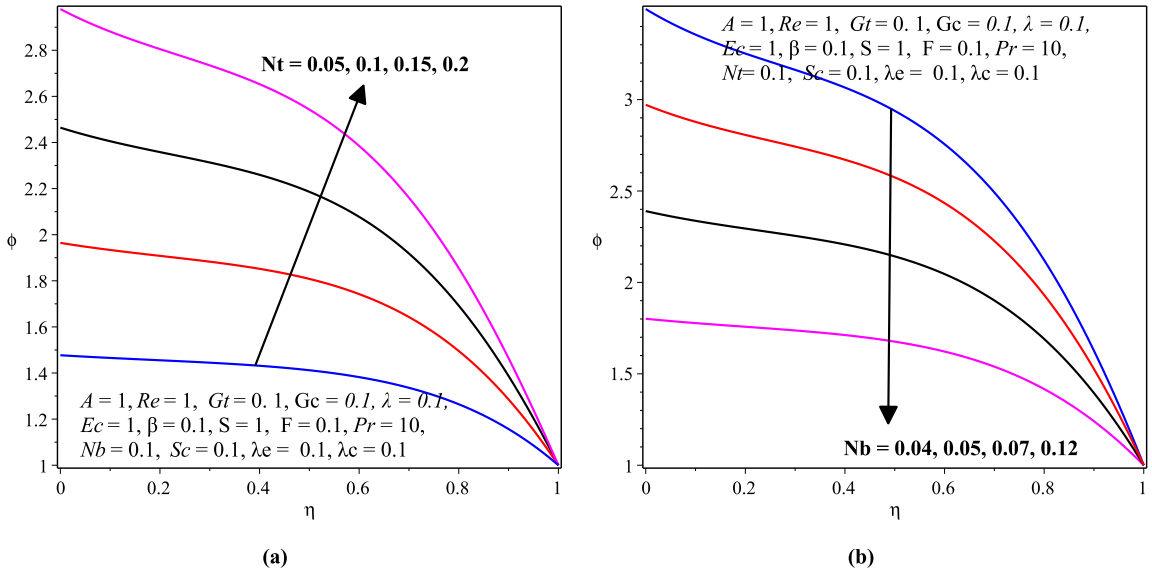

Figure 5.9: Effects of **(a)** *Nt* and **(b)** *Nb* on Concentration profile

Figures 5.12(a) and 5.12(b) depict the effects of the porous medium parameters S and F on the velocity profile. Figure 5.12(a) indicated that the velocity profile decreases significantly as the porous medium shape parameter S increase. From the literature, the studies in (Mahmoudi et al., 2020) and (Kasaeian et al., 2017) reported similar results. The reason behind this result is the fact that as the value of S increases, the porous medium permeability decreases which should naturally dampens the fluid flow and thus the observed decline in the

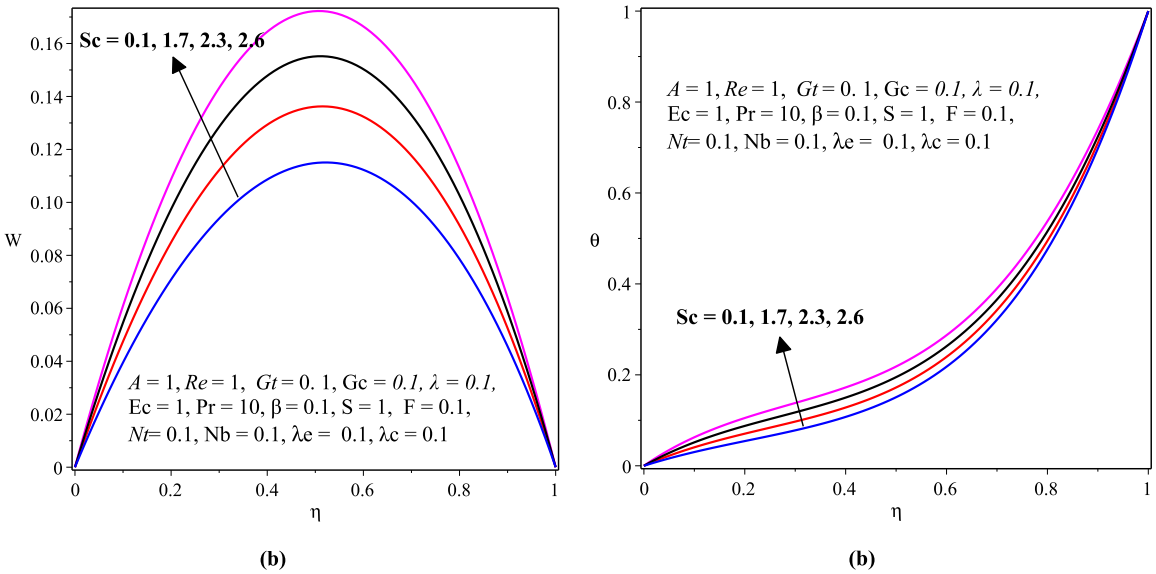

Figure 5.10: **(a)** Velocity and **(b)** Temperature profiles with varying Sc

magnitude of fluid velocity. In figures 5.12(b), it is observed that the fluid velocity profile decreases with increasing values of the Forchheimer number F which is also known as inertial resistance parameter. Physically, large values of F implies the stronger resistant inertial force in the direction normal to the fluid flow which is due to the intensive dimensionless drag force coefficient b since $F = \frac{ba}{\rho\sqrt{K}}$. For higher values of b stronger resistivity inertial force is effective within the fluid flow so that the velocity becomes lessen.

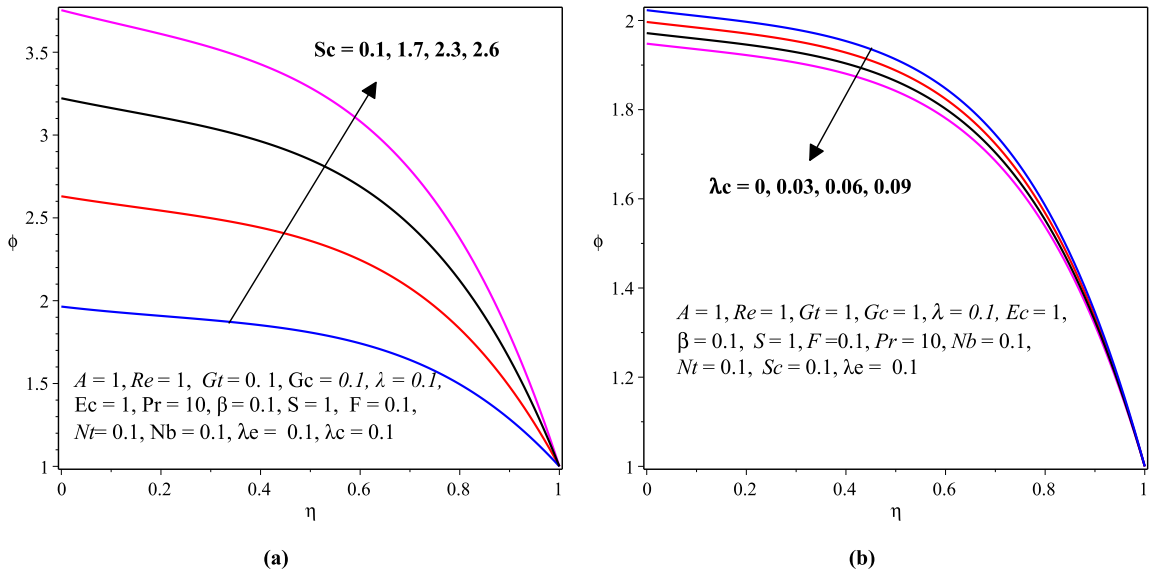

Figure 5.11: Effects of **(a)** Sc and **(b)** λc on Concentration profile

The effects of the Eckert number Ec on the fluid temperature and concentration profiles are depicted in figures 5.13(a) and 5.13(b) respectively. From the figures, it is observed that as the magnitude of Ec increases the fluid temperature also increase. This result is similar to the one obtained in the papers (Mahmoudi et al., 2020) and (Whitaker, 1986).

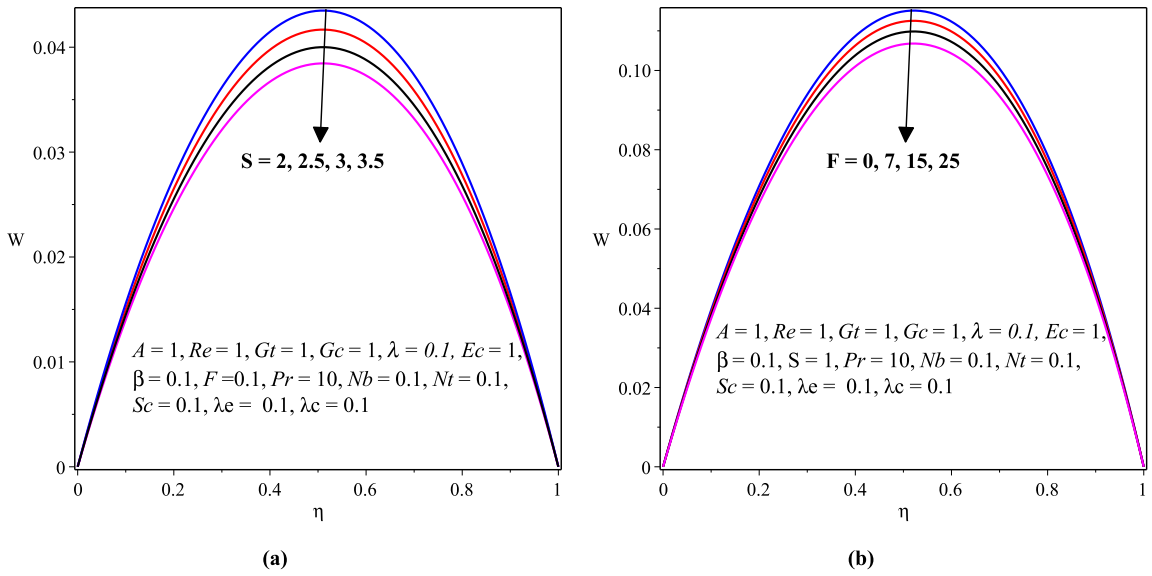

Figure 5.12: Effects of **(a)** S and **(b)** F on Velocity profile

Physically, the Eckert number Ec expresses the relationship between the flow boundary layer enthalpy difference and its kinetic energy which results in more heat to produce and hence Ec characterizes the viscous heating within the flow. Therefore, as the magnitude of Ec rises the viscous heating that will be enhanced within the flow resulting in the fluid temperature increment. Figure 5.13(b) displays the opposite phenomena for the concentration profile.

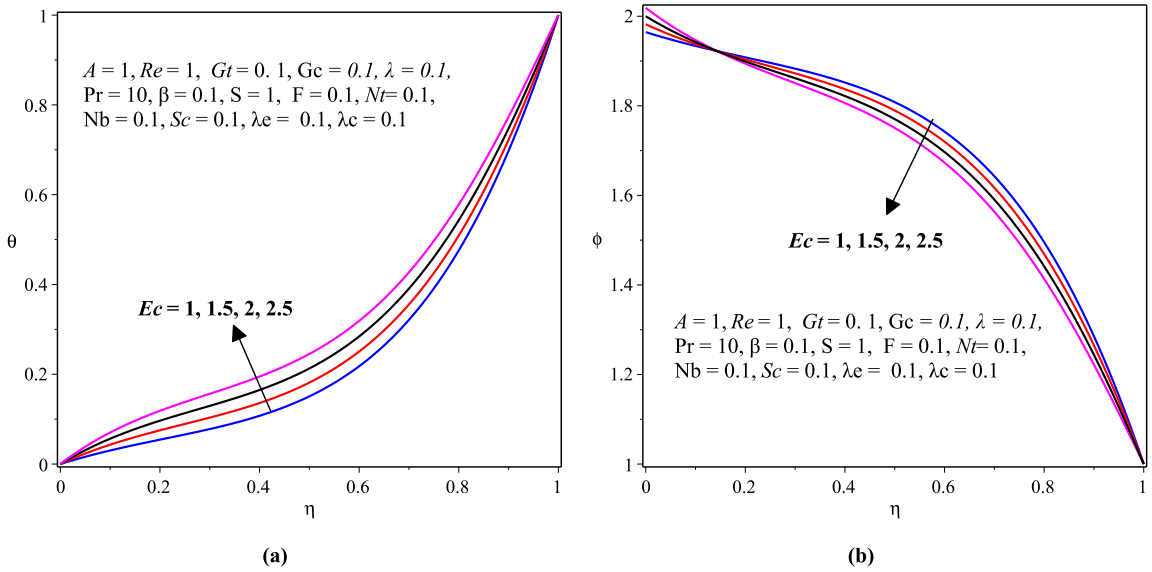

Figure 5.13: **(a)** Temperature and **(b)** Concentration profiles with varying Ec

Figures 5.14(a) and 5.14(b) are graphs that display the effects of the Prandtl number Pr on the temperature and concentration profiles. Accordingly, the larger values of Pr leads to a significant decrease in the temperature profile since higher values of Pr corresponds to low thermal diffusivity of the fluid (Pr and thermal diffusivity have inverse relationship) which reduces the rate at which heat is transported from the heated micro-channel walls

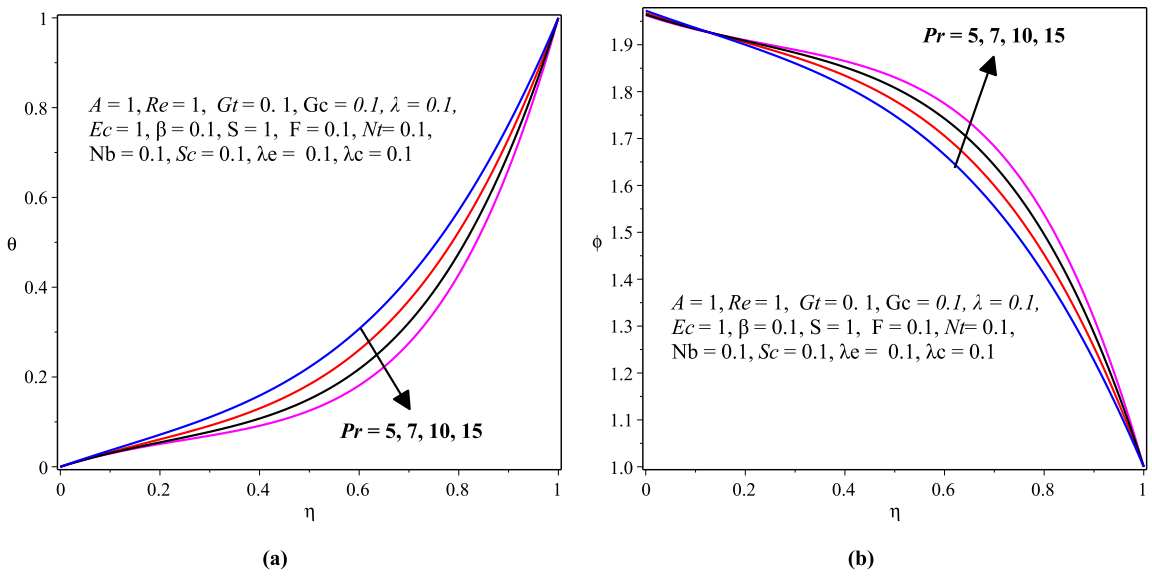

Figure 5.14: **(a)** Temperature and **(b)** Concentration profiles with varying Pr

into the fluid that was initially at zero temperature. Hence, as observed in figure 5.14(a) the fluid temperature decreases as the value of Pr increases. This result is similar to the one obtained by Whitaker (1986), Kasaeian et al. (2017) and Menni et al. (2018) but the opposite was observed in (Mahmoudi et al., 2020). On the other hand, figure 5.14(b) shows that the concentration profile increases with the Prandtl number Pr. Figures 5.15(a) and

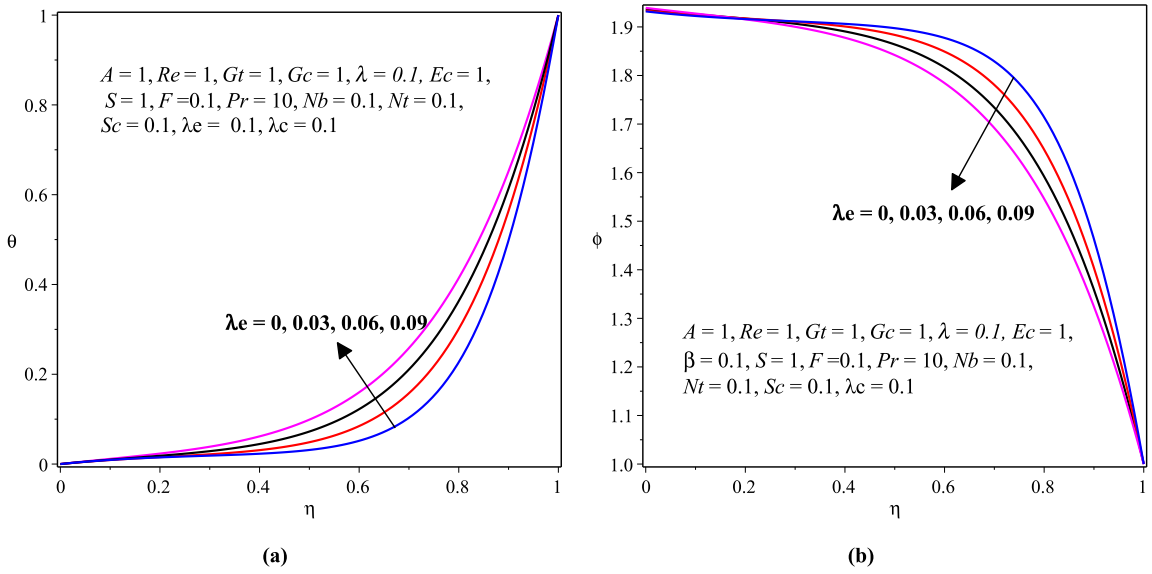

Figure 5.15: **(a)** Temperature and **(b)** Concentration profiles with varying λe

5.15(b) display the effects of the thermal relaxation parameter λ_e on the temperature and concentration profiles. Accordingly, figure 5.15(a) indicated that the larger values of λ_e leads to a significant increase in the temperature profile. Physically, thermal relaxation time is the time needed by the fluid particles to transfer the heat energy to the surrounding ones. Therefore, when λ_e increases the fluid particles need extra time to transfer heat to its adjacent

particles and so fluid temperature remains higher. That is, an increase in thermal relaxation parameter λ_e causes less transfer of heat from the fluid to surface of the microchannel. For $\lambda_e = 0$ the heat transfers slowly throughout the material. Hence temperature distribution is lower for $\lambda_e = 0$. Hence, the Cattaneo–Christov heat flux aspect is constructive in high heat flow process as compared to that of the classical Fourier's law of heat conduction. The same findings were reported by Mahanthesh et al. (2018) and Nayak et al. (2021). The opposite scenario was observed on the concentration profile with λ_e as depicted in figure 5.15(b).

5.2 The Wall Shear Stress, Wall Heat Transfer and Mass Transfer Rates

5.2.1 The Wall Shear Stress: Skin Friction Coefficient

The effects of pertinent parameters on the wall shear stress at the left wall $\eta = 0$ and at the right wall $\eta = 1$ are illustrated in figures 5.16(a)–5.18(b). Consequently, from these graphs it can be observed that the wall shear stress, coefficient of skin friction C_f (at both left and right walls) shows an increasing behavior with increasing values the Eckert number Ec, the Forchiemer number F and the pressure gradient parameter A for varying scaled values of the suction/injection Reynolds number Re. The results in the works of Mahmoudi et al. (2020) and Whitaker (1986) are similar with the outcomes of our research. The thermal Grashof number Gt shows a decreasing effect on C_f (at both left and right walls) for varying scaled values of the suction/injection Reynolds number Re. In addition, C_f increases as the values of the variable viscosity parameter λ increases at the left wall of the micro-channel $\eta = 0$ (see figure 5.18(a)) whereas C_f decreases with increasing values of the variable viscosity parameter λ at the right wall $\eta = 1$ (see figure 5.18(b)). However, the Casson fluid parameter β has shown the opposite effects at the left wall and the right wall of the microchannel as presented in figures 5.16(a) and 5.16(b).

5.2.2 The Wall Heat Transfer Rate: Nusselt Number

The effects of prominent governing flow parameters on the wall heat transfer rate at the left wall $\eta = 0$ and at the right wall $\eta = 1$ are portrayed in figures 5.19(a)–5.22(b). Accordingly, from these graphs we can see that the wall heat transfer rate, the Nusselt number Nu at both left and right walls shows an increasing behavior with increasing values of the variable viscosity parameter λ and the Eckert number Ec for varying scaled values of the suction/injection Reynolds number Re. This result is similar to the one obtained by Mahmoudi et al. (2020). The Nusselt number Nu at left wall of the microchannel has shown an increasing pattern with increasing values of the Casson fluid parameter β, pressure gradient parameter A, Prandtl number Pr and thermophoresis parameter Nt but it has shown a de-

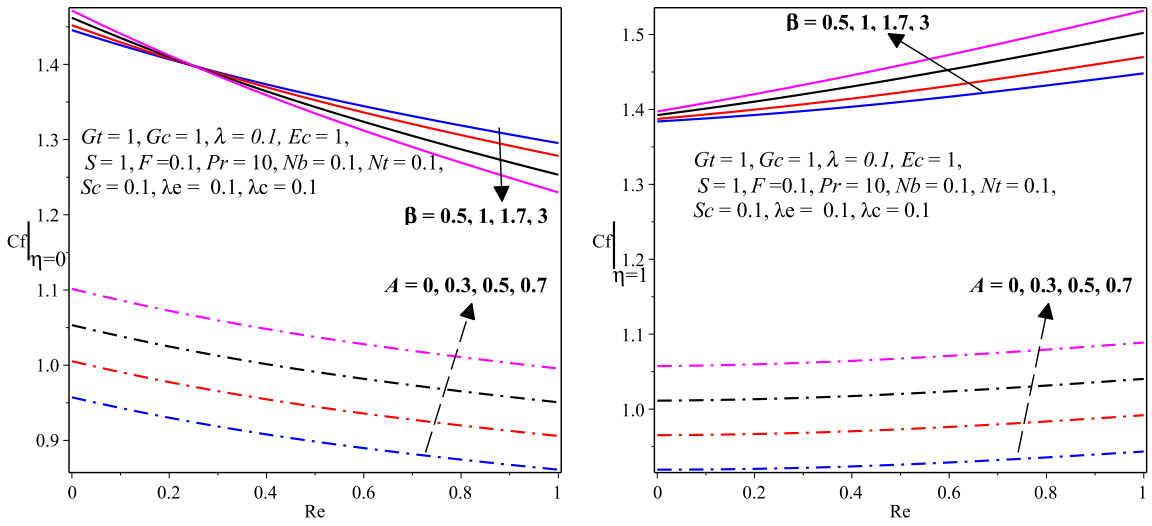

Figure 5.16: **(a)** Skin friction at $\eta = 0$ and **(b)** Skin friction at $\eta = 1$ with varying β, A and Re

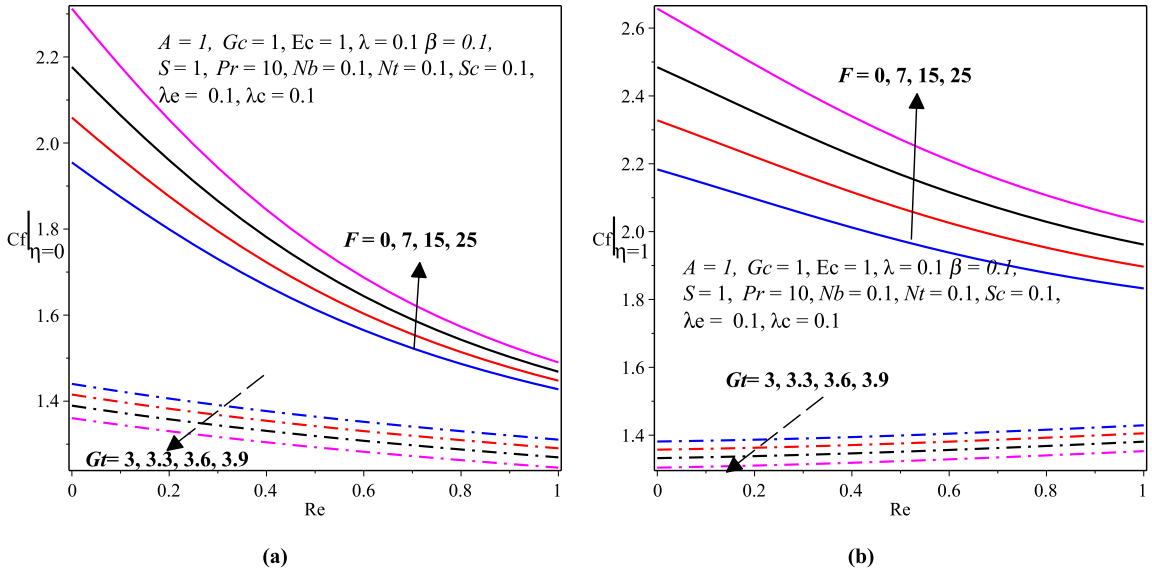

Figure 5.17: **(a)** Skin friction at $\eta = 0$ and **(b)** Skin friction at $\eta = 1$ with varying Gt, F and Re

creasing trend at the right wall of the microchannel. Nevertheless, the Nusselt number Nu at left wall of the microchannel has shown a decreasing pattern with increasing values of the Brownian motion parameter Nb and the thermal relaxation parameter λ_e but it has shown an increasing trend at the right wall of the microchannel.

5.2.3 The Wall Mass Transfer Rate: Sherwood Number

The effects of governing flow parameters on the wall mass transfer rate at the left wall $\eta = 0$ and at the right wall $\eta = 1$ are given in figures 5.23(a)–5.26(b). As a result, these graphs

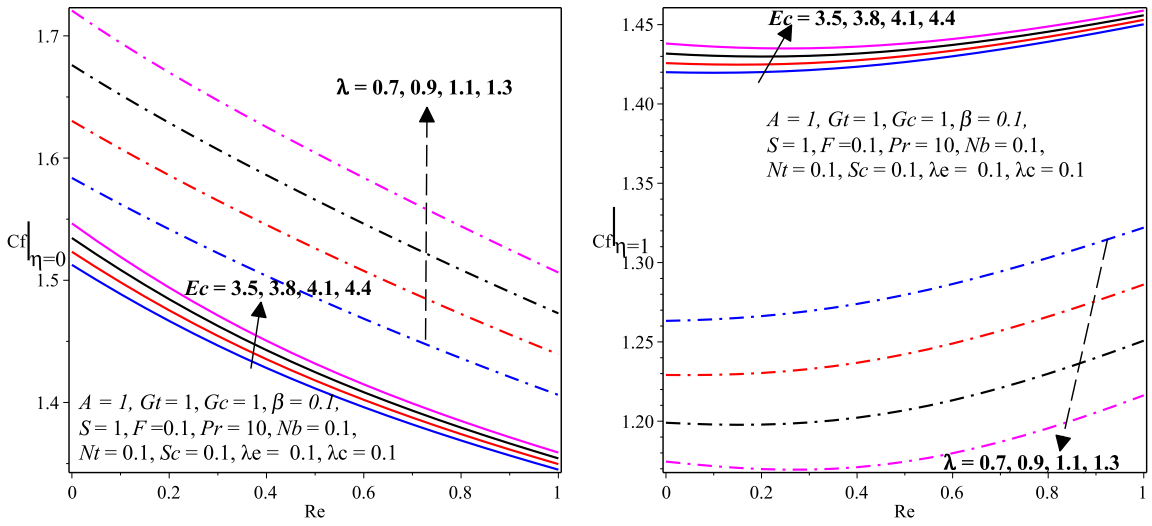

Figure 5.18: **(a)** Skin friction at $\eta = 0$ and **(b)** Skin friction at $\eta = 1$ with varying Ec, λ and Re

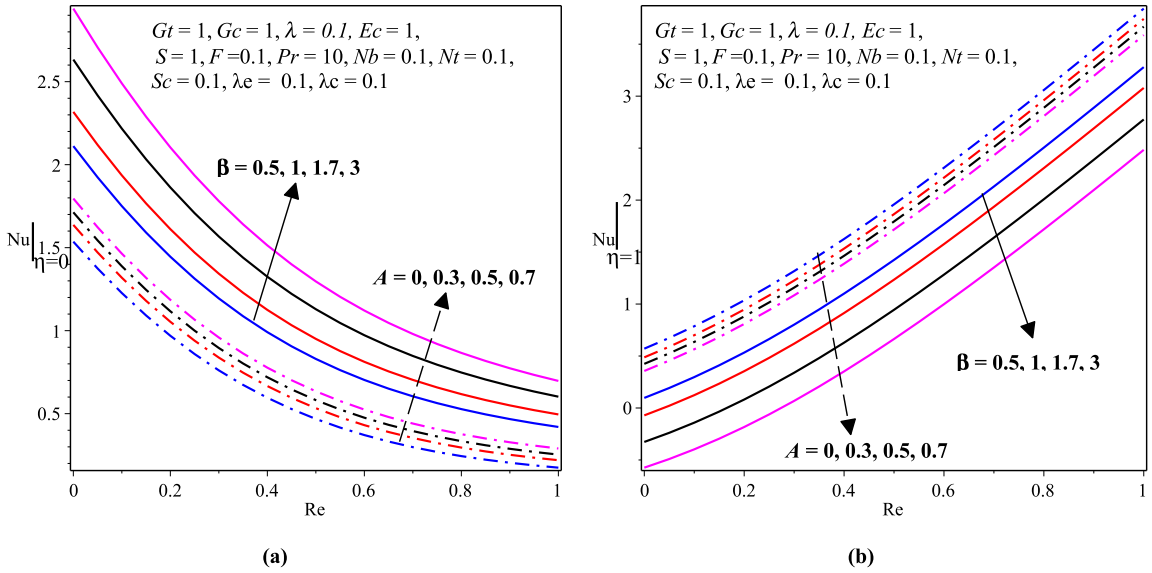

Figure 5.19: **(a)** Nusselt number at $\eta = 0$ and **(b)** Nusselt number at $\eta = 1$ with varying β, A and Re

depict that the wall mass transfer rate, Sherwood number Sh at both left and right walls shows an increasing trend with increasing values of the Eckert number Ec, variable viscosity parameter λ and the Schmidt number Sc for varying scaled values of the suction/injection Reynolds number Re. Nonetheless, the thermal relaxation parameter λ_e and the concentration relaxation parameter λ_c have shown a decreasing effect on Sh at both walls of the micro-channel.The Sherwood number Sh at left wall of the microchannel has shown an increasing pattern with increasing values of the Casson fluid parameter β, pressure gradient parameter A, and thermophoresis parameter Nt but it has shown a decreasing trend at the right wall of the microchannel.

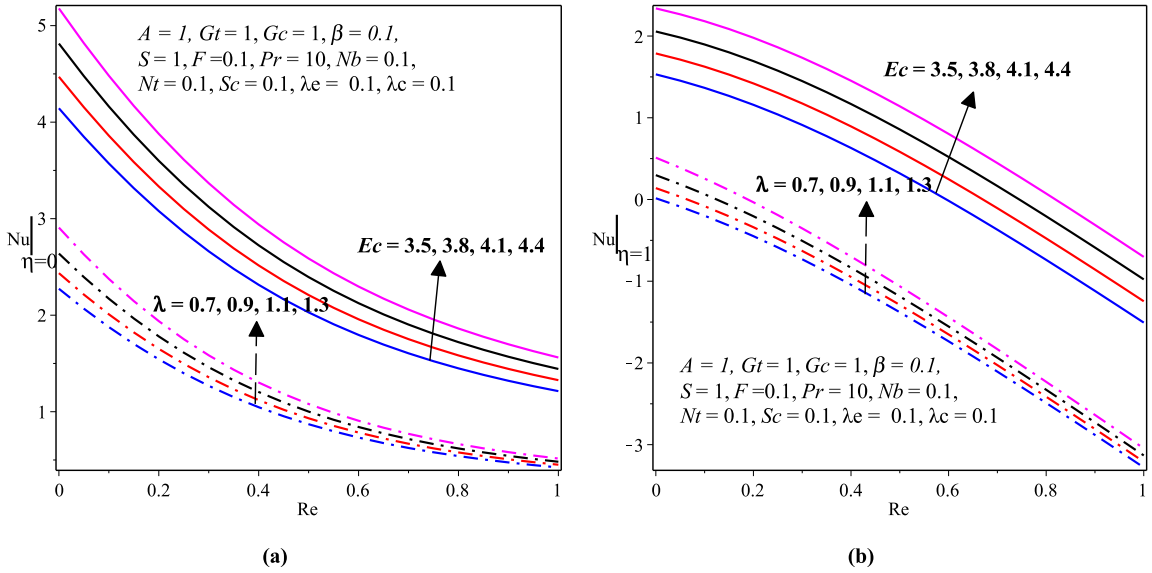

Figure 5.20: **(a)** Nusselt number at $\eta = 0$ and **(b)** Nusselt number at $\eta = 1$ with varying Ec, λ and Re

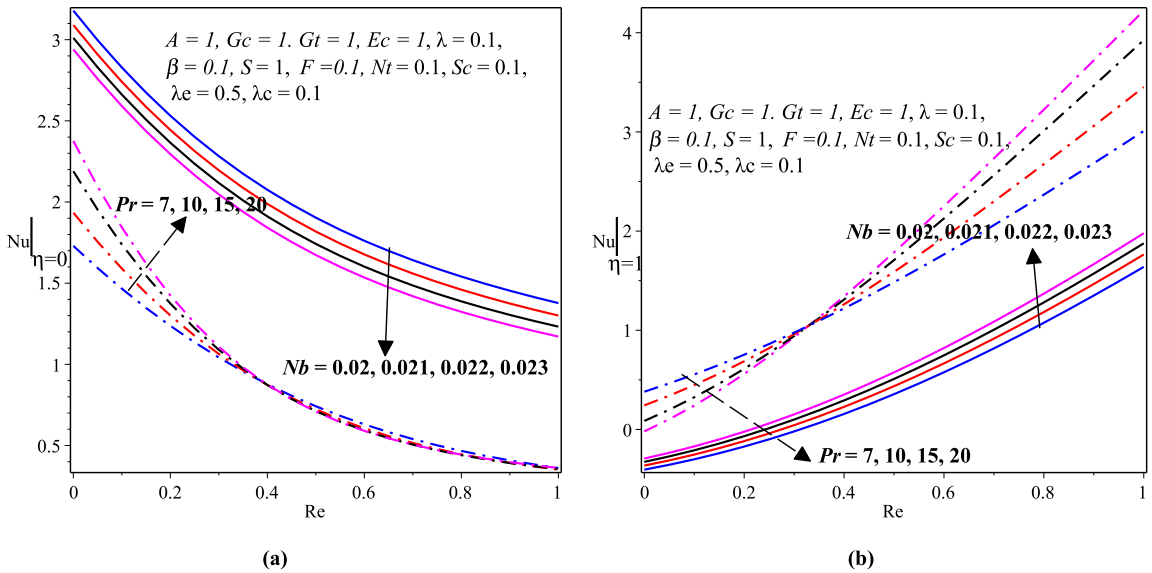

Figure 5.21: **(a)** Nusselt number at $\eta = 0$ and **(b)** Nusselt number at $\eta = 1$ with varying Pr, Nb and Re

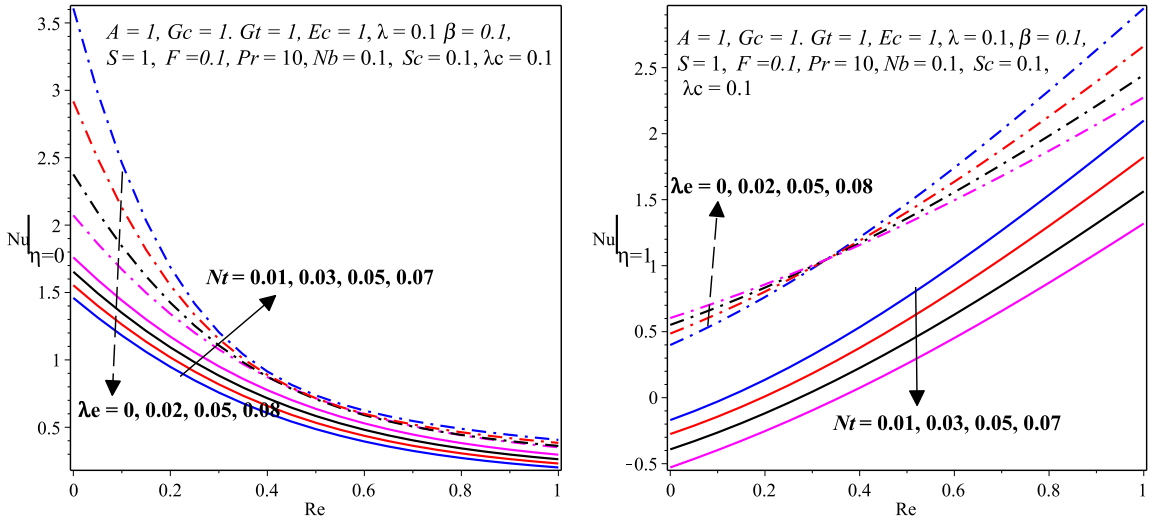

Figure 5.22: **(a)** Nusselt number at $\eta = 0$ and **(b)** Nusselt number at $\eta = 1$ with varying Nb, λe and Re

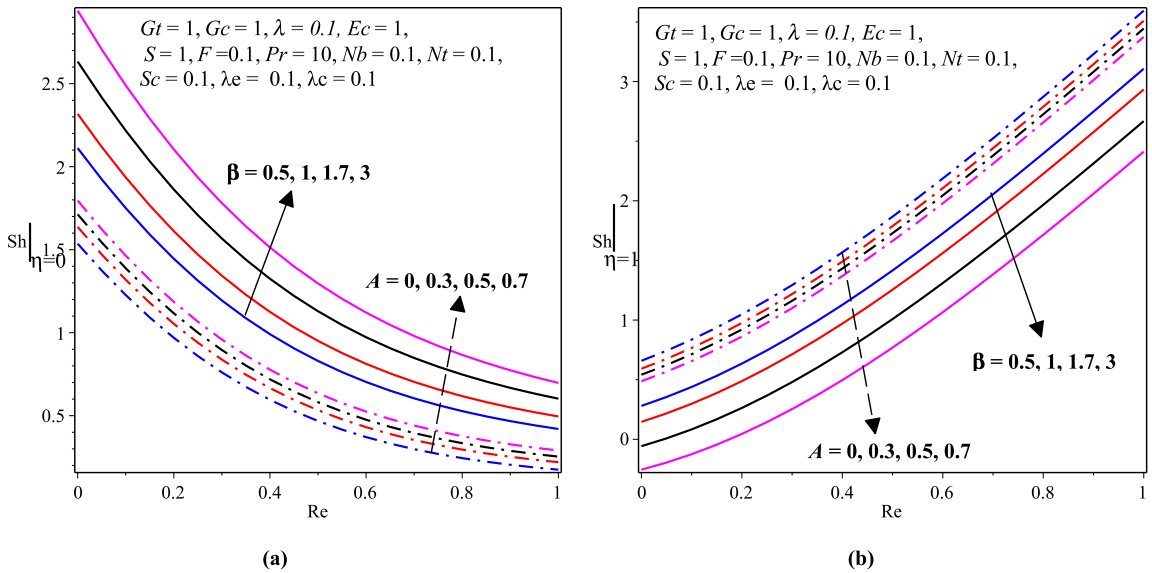

Figure 5.23: **(a)** Sherwood number at $\eta = 0$ and **(b)** Sherwood number at $\eta = 1$ with varying β, A and Re

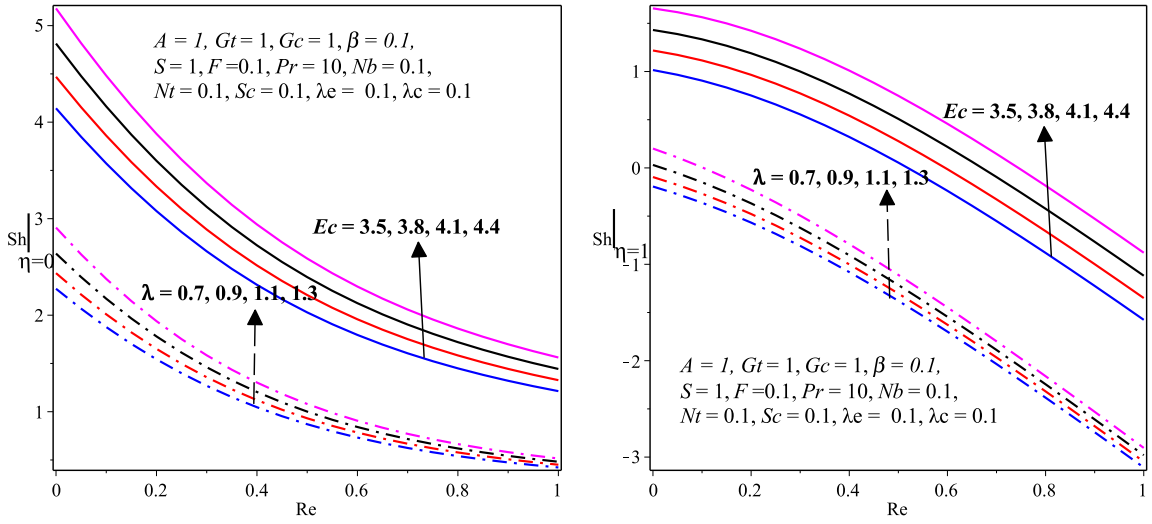

Figure 5.24: **(a)** Sherwood number at $\eta = 0$ and **(b)** Sherwood number at $\eta = 1$ with varying Ec, λ and Re

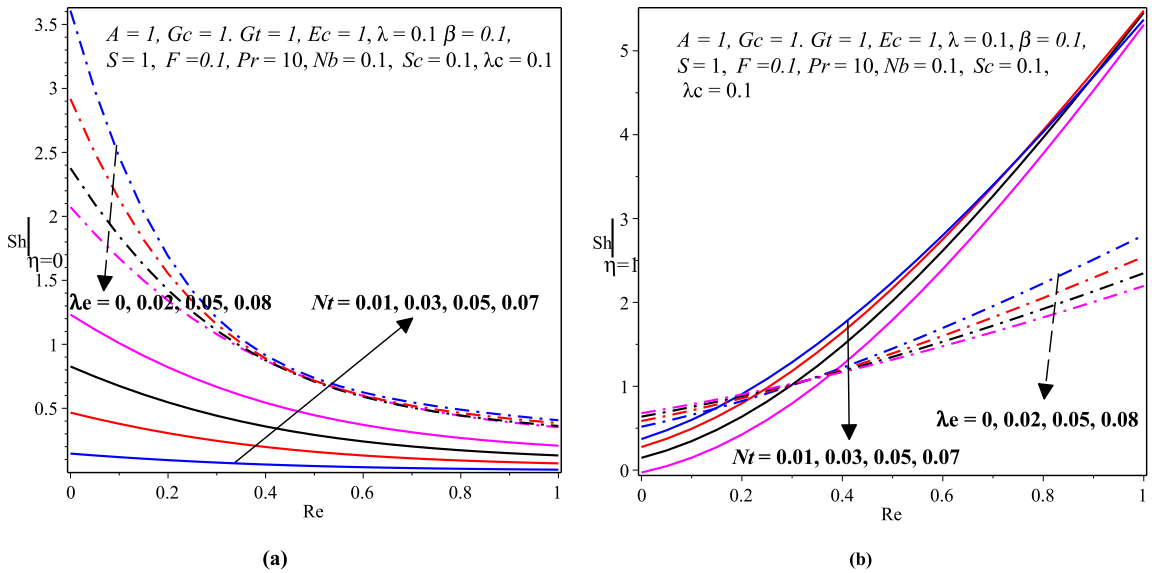

Figure 5.25: **(a)** Sherwood number at $\eta = 0$ and **(b)** Sherwood number at $\eta = 1$ with varying Nt, λe and Re

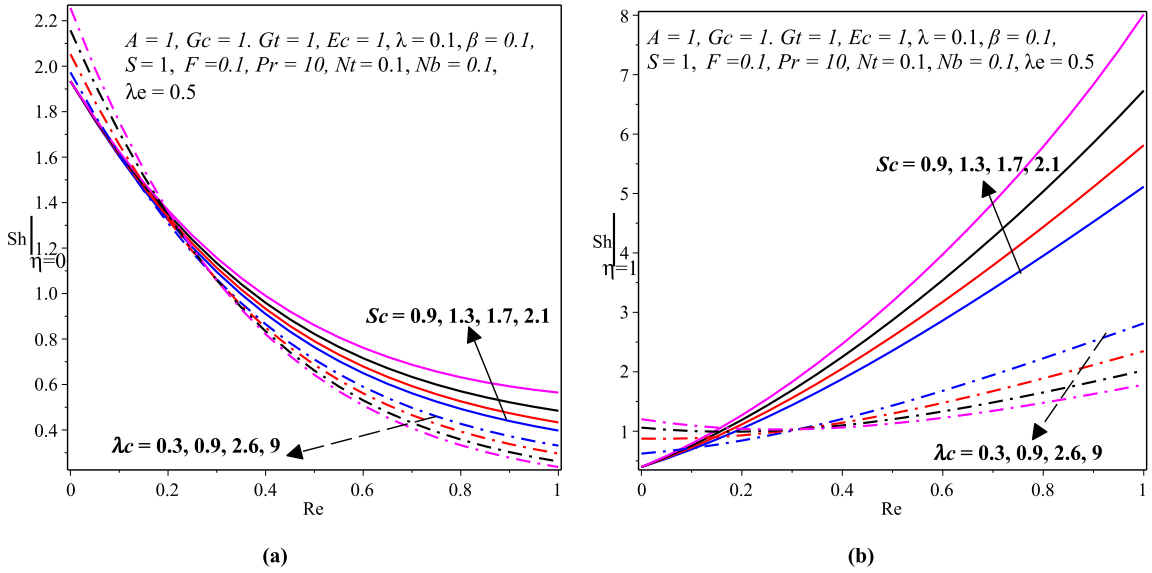

Figure 5.26: **(a)** Sherwood number at $\eta = 0$ and **(b)** Sherwood number at $\eta = 1$ with varying Sc, λc and Re

CHAPTER 6

SUMMARY, CONCLUSIONS AND RECOMMENDATIONS

6.1 Summary

The heat and mass transfer characteristics as well as the hydrodynamical properties of Casson nanofluid flow through microchannels in the presence of porous media with non-uniform permeable walls temperature have large scale utilization in industries, engineering and biotechnology. Therefore, this research project considered the analysis of Casson nanofluid flow as well as heat and mass transfer characteristics with variable viscosity. The flow was generated due to the axial pressure gradient, suction/injection and buoyancy forces. The Buongiorno's nanofluids flow model (two-phase model) was used to examine the effects of the Brownian diffusion and the thermophoresis diffusion of nanoparticles while the Darcy-Forchheimer model was considered to study the interaction between the nanofluid and the porous media.

The highly non-linear partial differential equations for momentum, energy and concentration were formulated, non-dimensionalized and then solved using the Keller–Box method. Finally, the numerical solutions were displayed via graphs to indicate the effects of the pertinent parameters on the velocity, temperature, species concentration, skin-friction coefficient, heat transfer rate (Nusselt number) and mass transfer rate (Sherwood number).

6.2 Conclusions

This research project presented the investigation of hydrodynamic and thermal behaviours of Casson nanofluid flow in microchannels filled with porous media. Therefore, depending on the results obtained from the analysis presented in this research project, the key conclusions are given as follows.

- Both velocity and temperature profiles have shown an increasing behavior with increasing values of the Casson fluid parameter β, variable viscosity parameter λ, Eckert number Ec, thermal Grashof number Gt, the solutal Grashof number Gc, Schmidt number Sc, thermophoresis parameter Nt, and thermal relaxation parameter λ_e.

- The Brownian motion parameter Nb has shown an opposite effect on the velocity and temperature profiles.

- The concentration profile has indicated an increasing trend with increasing values of the Prandtl number Pr, the Schmidt number Sc and the thermophoresis parameter Nt.
- The skin friction coefficient C_f at both sides of the microchannel walls is large for higher vales of the pressure gradient parameter A, the Eckert number Ec, Forchheimer number F and suction/injection parameter Re.
- Both Casson fluid parameter β and variable viscosity parameter λ have shown opposite effects on the skin friction coefficient C_f at the left and right walls of the microchannel.
- The Nusselt number Nu at both sides of the microchannel walls has shown an increasing pattern with an increasing values of the Eckert number Ec, variable viscosity parameter λ and suction/injection parameter Re.
- Both Casson fluid parameter β and thermal relaxation parameter λ_e have indicated opposite effects on the Nusselt number Nu at the left and right walls of the microchannel.
- The Sherwood number Sh at both sides of the microchannel walls has shown an increasing pattern with an increasing values of the Eckert number Ec, variable viscosity parameter λ, Schmidt number Sc and suction/injection parameter Re.

6.3 Recommendation and Suggestions for Future Research

6.3.1 Recommendation

The findings of this research project are useful for food processing industries and biomedical technology from the perspective of heat transfer systems design. Thus, integrating the findings of the current theoretical model with experimental investigations can improve the existing design in cooling systems by making use of variable viscosity Casson nanofluid trough a permeable microchannel filled with a porous medium.

6.3.2 Suggestions for Future Research

The results obtained in the current research project can be extended to different flow problems in the following ways.

- The effects of the body forces like Lorentz and Coriolis forces can be included by considering MHD and rotating Casson nanofluid.
- The Soret and Dufour effects (thermal-diffusion and diffusion-thermo) with slip and hall current can also be considered.
- One can also consider the entropy generation analysis with heat generation/absorption.

REFERENCES

Ahadi, A., Antoun, S., Saghir, M., and Swift, J. (2019). Computational fluid dynamic evaluation of heat transfer enhancement in microchannel solar collectors sustained by alumina nanofluid. *Energy Storage*, 1(2):e37.

Bergman, T., Incropera, F., DeWitt, D., and Lavine, A. (2011). *Fundamentals of Heat and Mass Transfer*. Wiley & Sons.

Buongiorno, J. (2006). Convective transport in nanofluids. *ASME J. Heat Transfer*, 128(3):240–250.

Casson, N. (1959). A flow equation for pigment-oil suspensions of the printing ink type. *Rheol. Disperse Syst. Pergamon Press*, pages 84–104.

Cebeci, T. and Bradshaw, P. (1984). *Physical and Computational Aspects of Convective Heat Transfer*. springer–verlag.

Choi, S. (1995). Enhancing thermal conductivity of fluids with nanoparticles. *ASME Int Mech Eng.*, 66:99–105.

Delisle, C., Welsford, C., and Saghir, M. (2019). Forced convection study with microporous channels and nanofluid: experimental and numerical. *Journal of Thermal Analysis and Calorimetry*, 140(6):1205–1214.

Dewan, A. and Srivastava, P. (2015). A review of heat transfer enhancement through flow disruption in a microchannel. *Journal of Thermal Science*, 24(3):203–214.

Endalew, M., Sarkar, S., Seth, G, S., and Makinde, O. (2018). Dual-phase-lag heat transfer model in hydromagnetic second grade flow through a microchannelfilled with porous material: A time-bound analysis. *Revue des composites et des matériaux avancés*, 28:173–194.

Gireesha, B., Srinivasa, C., Shashikumar, N., Macha, M., Singh, J., and Mahanthesh, B. (2019). Entropy generation and heat transport analysis of Casson fluid flow with viscous and Joule heating in an inclined porous microchannel. *Proc I Mech E Part E: J Process Mechanical Engineering*, 0(0):1–12.

Hari Krishna, Y., Venkata Ramana Reddy, G., and Makinde, O. (2018). Chemical reaction effect on mhd flow of Casson fluid with porous stretching sheet. *Defect and Diffusion Forum*, 389:100–109.

Hayat, T., Saeed, Y., Alsaedi, A., and Asad, S. (2015). Effects of convective heat and mass transfer in flow of Powell-Eyring fluid past an exponentially stretching sheet. *journal of PLoS ONE*, 10(9).

Holman, J. (2010). *Heat Transfer: Tenth Edition*. McGraw-Hill Education.

Kasaeian, A., Daneshazarian, R., Mahian, O., Kolsi, L., Chamkha, A., Wongwises, S., and Pop, I. (2017). Nanofluid flow and heat transfer in porous media: A review of the latest developments. *International Journal of Heat and Mass Transfer*, 107:778–791.

Kmiotek, M. and Kucab-Pietal, A. (2018). Influence of slim obstacle geometry on the flow and heat transfer in microchannels. *Bulletin of the Polish Academy of Technical Sciences*, 66(2):111–118.

Kumar, R., Islam, M., and Hasan, M. (2014). A review of experimental investigations on heat transfer characteristics of single phase liquid flow in microchannels. *International Journal of Advanced Mechanical Engineering*, 4(1):115–120.

Mahanthesh, B., Makinde, O., Gireesha, B., Krupalakshmi, K., and Animasaun, I. (2018). Two-phase flow of dusty Casson fluid with Cattaneo-Christov heat flux and heat source past a cone, wedge and plate. *Defect and Diffusion Forum*, 387:625–639.

Mahmoudi, Y., Hooman, K., and Vafai, K. (2020). *Convective Heat Transfer in Porous Media*. Taylor & Francis Group. CRC Press.

Makinde, O. (2018). Heat transfer in variable viscosity microchannelflow of EG-water/Ag nanofluids with convective cooling. *Defect and Diffusion Forum*, 387:510–522.

Mehendale, S., Jacobi, A., and Shah, R. (2000). Fluid flow and heat transfer at micro- and meso-scales with applications to heat exchanger design,. *Appl. Mech. Rev.,*, 53:175–193.

Mehmood, R., Nayak, M., Sher Akbar, N., and Makinde, O. (2019). Effects of thermal-diffusion and diffusion-thermoon oblique stagnation point flow of couple stress Casson fluid over a stretched horizontal riga plate with higher order chemical reaction. *Journal of Nanofluids*, 8(1):1–9.

Menni, Y., Chamkha, A., and Azzi, A. (2018). Nanofluid transport in porous media: a review. special topics & reviews in porous media. *An International Journal*, 9(4):1–16.

Moon, J., Pacheco, J., and Pacheco-Vega, A. (2019). Heat transfer enhancement in wavy microchannels: Effect of block material. *Proceedings of the 4th World Congress on Momentum, Heat and Mass Transfer*, MHMT'19(ENFHT120):1–11.

Mukhopadhyay, S., Bhattacharyya, K., and Hayat, T. (2013). Exact solutions for the flow of Casson fluid over a stretching surface with transpiration and heat transfer effects. *Chin. Phys. B*, 22:114701–114721.

Nayak, M., Pandey, V., Shaw, S., M. O., Ramadan, K., Henda, M., and Tlili, I. (2021). Thermo-fluidic significance of non Newtonian fluid with hybrid nanostructures. *Case Studies in Thermal Engineering*, pages 1–38.

Niazi, M. and Xu, H. (2020). Modelling two-layer nanofluid flow in a microchannelwith electro-osmotic effects by means of the Buongiorno's model. *Applied Mathematics and Mechanics (English Edition). Shanghai University and Springer-Verlag GmbH Germany*, 41(1):83–104.

Prameela, M., Venkateswarlu, M., and Makinde, O. (2019). Influence of heat generation and viscous dissipation on hydromagnetic fully developed natural convection flow in a vertical microchannel. *J. Nanofluids*, 8(7):1506–1516.

Reddy, K., Makinde, O., and Reddy, M. (2018). Thermal analysis of mhd electro-osmotic peristaltic pumping of casson fluid through a rotating asymmetric microchannel. *Indian J Phys.*, 92(11):1439–1448.

Reddy, K., Reddy, M., and Makinde, O. (2019). Thermophoresis and Brownian motion effects on MHD electro-osmotic jeffrey nanofluid peristaltic flow in asymmetric rotating microchannel. *J. Nanofluids*, 8(2).

Roja, A., Gireeesha, B., and Nagaraja, B. (2021). Irreversibility investigation of Casson fluid flow in an inclined channel subject to a Darcy–Forchheimer porous medium: a numerical study. *Applied Mathematics and Mechanics (English Edition)*, 42(1):95–108.

Saleel, C., Algahtani, A., Badruddin, I., Khan, T., Kamangar, S., and Abdelmohimen, M. (2019). Pressure-driven electro-osmotic flow and mass transport in constricted mixing microchannels. *Journal of Applied Fluid Mechanics*, 13(2):429–441.

Shahrestani, M., Maleki, A., Shadloo, M., and Tlili, I. (2020). Numerical investigation of forced convective heat transfer and performance evaluation criterion of Al_2O_3/water nanofluid flow inside an axisymmetric microchannel. *Symmetry*, 120.

Sharaf, O., Al-Khateeb, A., Kyritsis, D., and Abu-Nada, E. (2019). Numerical investigation of nanofluid particle migration and convective heat transfer in microchannels using an Eulerian-Lagrangian approach. *J. Fluid Mech.*, 878:62–97.

Shashikumar, N., Prasannakumara, B., Gireesha, B., and Makinde, O. (2018). Thermodynamics analysis of MHD Casson fluid slip flow in a porous microchannel with thermal radiation. *Diffusion Foundations*, 16:120–139.

Subramanian, K., Rao, T., and Balakrishnan, A. (2020). *Nanofluids and Their Engineering Applications*. Taylor & Francis Group. CRC Press.

Thammanna, G., Ganesh Kumar, K., Gireesha, B., Ramesh, G., and Prasannakumara, B. (2017). Magnetohydrodynamic analysis on stretched flow of couple stress Casson fluid with chemical reaction. *Results in Physics*, 7:4104–4124.

Tuckerman, D. and Pease, R. (1981). High-performance heat sinking for VLSI. *IEEE Electron device letters*, 2(5):126–129.

Ullah, I., Abdullah Alkanhal, T., Sharidan, S., Sooppy Nisar, K., Khan, I., and Makinde, O. (2019). MHD slip flow of Casson fluid along a nonlinear permeable stretching cylinder saturated in a porous medium with chemical reaction, viscous dissipation and heat generation/absorption. *Symmetry*, 11:351–371.

Vafai, K. (2005). *Handbook of Porous Media. 2nd ed.* Taylor & Francis.

Venkateswarlu, M., Makinde, O., and Lakshmi, D. (2019). Influence of thermal radiation and heat generation on steady hydromagnetic flow in a vertical micro-porous-channel in presence of suction/injection. *Journal of Nanofluids*, 8(5):1010–1019.

Waghmare, P., Mithra, S., Mather, A., and McLaughlin, J. (2008). Modeling, fabrication and simulation of microfilters. *ECI International Conference on Heat Transfer and Fluid Flow in Microscale*, pages 260–277.

Whitaker, S. (1986). Flow in porous media I: A theoretical derivation of Darcy's law. *Transport in Porous Media*, 1:3–25.